



January 2021

## Large Scale Low Speed Wind Tunnel

Ty Nygaard

[How does access to this work benefit you? Let us know!](#)

Follow this and additional works at: <https://commons.und.edu/theses>

---

### Recommended Citation

Nygaard, Ty, "Large Scale Low Speed Wind Tunnel" (2021). *Theses and Dissertations*. 4176.  
<https://commons.und.edu/theses/4176>

This Thesis is brought to you for free and open access by the Theses, Dissertations, and Senior Projects at UND Scholarly Commons. It has been accepted for inclusion in Theses and Dissertations by an authorized administrator of UND Scholarly Commons. For more information, please contact [und.common@library.und.edu](mailto:und.common@library.und.edu).

LARGE SCALE LOW SPEED WIND TUNNEL

by

Ty Nicholas Nygaard  
Bachelor of Science Mechanical Engineering, University of North Dakota, 2020

A Thesis

Submitted to the Graduate Faculty

of the

University of North Dakota

In partial fulfillment of the requirements

for the degree of

Master of Science  
Mechanical Engineering

Grand Forks, North Dakota

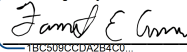
December

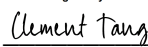
2021

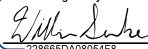
Copyright © 2021 Ty Nygaard

Name: Ty Nygaard  
Degree: Master of Science

This document, submitted in partial fulfillment of the requirements for the degree from the University of North Dakota, has been read by the Faculty Advisory Committee under whom the work has been done and is hereby approved.

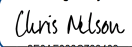
DocuSigned by:  
  
1BC509CCDA2B4C0...  
Dr. Forrest Ames, Ph.D.

DocuSigned by:  
  
0F5827F8551341B...  
Dr. Clement Tang, Ph.D.

DocuSigned by:  
  
228665DA09054F8...  
Dr. William Semke, Ph.D.

\_\_\_\_\_  
  
\_\_\_\_\_  
  
\_\_\_\_\_

This document is being submitted by the appointed advisory committee as having met all the requirements of the School of Graduate Studies at the University of North Dakota and is hereby approved.

DocuSigned by:  
  
2E0A7088C733403...  
Chris Nelson  
Dean of the School of Graduate Studies  
  
12/9/2021  
\_\_\_\_\_  
Date

## PERMISSION

Title            Large Scale Low Speed Wind Tunnel

Department    Mechanical Engineering

Degree         Master of Science

In presenting this thesis in partial fulfillment of the requirements for a graduate degree from the University of North Dakota, I agree that the library of this University shall make it freely available for inspection. I further agree that permission for extensive copying for scholarly purposes may be granted by the professor who supervised my thesis work or, in his absence, by the Chairperson of the department or the dean of the School of Graduate Studies. It is understood that any copying or publication or other use of this thesis or part thereof for financial gain shall not be allowed without my written permission. It is also understood that due recognition shall be given to me and to the University of North Dakota in any scholarly use which may be made of any material in my thesis.

Ty Nygaard  
12/09/2021

## TABLE OF CONTENTS

TABLE OF FIGURES.....	VII
TABLE OF TABLES.....	IX
NOMENCLATURE.....	13
CHAPTER.....	14
I.    INTRODUCTION.....	14
a.    Objectives .....	15
II.   BACKGROUND.....	17
III.  EXPERIMENTAL AND COMPUTATIONAL APPROACH.....	24
a.    Analytical Development .....	24
i.    Fan Mass Flow Rate.....	24
ii.   Subsonic Nozzle Contraction .....	25
iii.  Flow Conditioning.....	25
b.    CFD Simulation Setup.....	27
i.    Geometry .....	27
ii.   Boundary Conditions.....	29
iii.  Mesh Interdependence Study.....	30
c.    Wind Tunnel Components.....	34
i.    Flow Conditioning.....	34
ii.   Inlet Contraction.....	39
iii.  Test Section .....	42
iv.   Test Cart.....	45
v.    Propeller Test Stand .....	47
vi.   Traversing Section.....	51
vii.  Fan Assembly.....	53
viii. Multi-Vane Diffuser .....	57
IV.  RESULTS AND DISCUSSION.....	59
a.    CFD Results.....	59
i.    Convergence Criterion .....	59
ii.   Postprocessing Results.....	60
b.    Expected Experimental Results Plan.....	63
i.    Validation of Inlet and Exit Flow .....	63

<b>ii. Test Cart .....</b>	<b>64</b>
<b>iii. Propeller Test Stand.....</b>	<b>64</b>
<b>iv. High Speed Camera Measurements .....</b>	<b>65</b>
<b>V. RECOMMENDATIONS .....</b>	<b>66</b>
<b>VI. CONCLUSION .....</b>	<b>68</b>
<b>REFERENCES.....</b>	<b>69</b>
<b>APPENDIX A .....</b>	<b>71</b>

## TABLE OF FIGURES

<b>Figure 1. Wireframe Isometric View of Wind Tunnel Geometry.....</b>	<b>14</b>
<b>Figure 2. Flow around a Propeller using Momentum Theory.....</b>	<b>22</b>
<b>Figure 3. CFD Geometry 2-D Side View.....</b>	<b>28</b>
<b>Figure 4. CFD Geometry 2-D Top View.....</b>	<b>28</b>
<b>Figure 5. Wireframe Isometric View of Wind Tunnel Geometry.....</b>	<b>29</b>
<b>Figure 6. CFD Geometry Arbitrary Mesh.....</b>	<b>31</b>
<b>Figure 7. CFD Geometry Intermediate Mesh.....</b>	<b>31</b>
<b>Figure 8. CFD Geometry Fine Mesh.....</b>	<b>32</b>
<b>Figure 9. Centerline Velocity Mesh Comparison.....</b>	<b>33</b>
<b>Figure 10. Flow Straightener Matrix Assembly.....</b>	<b>36</b>
<b>Figure 11. Mounting of Flow Straightener.....</b>	<b>36</b>
<b>Figure 12. Completed Flow Straightener.....</b>	<b>37</b>
<b>Figure 13. Fine Mesh Screen Stitching.....</b>	<b>38</b>
<b>Figure 14. Fine Mesh Screen Mounted.....</b>	<b>39</b>
<b>Figure 15. Inlet Nozzle Base Curve.....</b>	<b>40</b>
<b>Figure 16. Inlet Contraction 3-D Model.....</b>	<b>41</b>
<b>Figure 17. Constructed Inlet Contraction.....</b>	<b>42</b>
<b>Figure 18. Test Section Control Room.....</b>	<b>44</b>
<b>Figure 19. Constructed Test Section.....</b>	<b>45</b>
<b>Figure 20. Test Cart CAD Model.....</b>	<b>46</b>
<b>Figure 21. Constructed Test Cart without Plywood Top Sheet.....</b>	<b>47</b>
<b>Figure 22. Series 1780 Test Stand 25 kgf 100-amp: Single Motor.....</b>	<b>49</b>
<b>Figure 23. Assembled Series 1780 Test Stand 25 kgf 100-amp: Single Motor.....</b>	<b>50</b>
<b>Figure 24. Initial Traversing Mechanism Design.....</b>	<b>52</b>



<b>Figure 25. Fan Cart Assembly with Mounted Motor and Flywheel.....</b>	<b>53</b>
<b>Figure 26. Constructed Fan Assembly prior to Lift.....</b>	<b>55</b>
<b>Figure 27. Mounted Brackets into Concrete.....</b>	<b>56</b>
<b>Figure 28. Mounted Fan Assembly to Test Section.....</b>	<b>56</b>
<b>Figure 29. Constructed Multi-vane Diffuser Rear View.....</b>	<b>58</b>
<b>Figure 30. RMS Residuals Convergence of 1E-05.....</b>	<b>60</b>
<b>Figure 31. Velocity Streamlines at Midpoint in Test Section.....</b>	<b>61</b>
<b>Figure 32. Velocity Streamlines and Contours within Test Section and Diffuser.....</b>	<b>62</b>
<b>Figure 33. Pressure Contours at Midpoint in Test Section.....</b>	<b>63</b>

**TABLE OF TABLES**

**Table 1. Centerline Mesh Comparison Percent Error at 2.25 m.....33**

**Table 2. “S” Shape Curve Inlet Contraction Dimensions (1 of 3).....71**

**Table 3. “S” Shape Curve Inlet Contraction Dimensions (2 of 3).....72**

**Table 4. “S” Shape Curve Inlet Contraction Dimensions (3 of 3).....73**

## ACKNOWLEDGEMENTS

I wish to express my sincere appreciation to my thesis advisor Dr. Forrest Ames for his guidance and insight. I would also like to extend my appreciation to Dr. Clement Tang and Dr. William Semke for their continued support throughout my studies.

I would like to thank the University of North Dakota College of Engineering and Mines as well as the Institute for Energy Studies for the initial support of this project. I am grateful for all the relationships I was able to build with both faculty and students around campus. My success would not have been possible without their support.

To my beautiful wife, Taylor.

## ABSTRACT

This thesis documents the design, construction, and functionality of a large-scale wind tunnel designed to test and investigate losses of full size and scaled UAV propellers and rotors. The wind tunnel has been developed as an open circuit wind tunnel but will later be converted to a closed-circuit wind tunnel. A computational model of the wind tunnel was developed to help assess issues related to the 180 degree turns at both the inlet and exit diffuser and the associated losses and flow distortion. Results from analytical solutions and the computational model have been compared against one another and indicate sufficient agreement. The wind tunnel is composed of major components which are the flow conditioning, inlet contraction, test section, test cart, propeller test stand, traversing section, fan assembly, and multi-vane diffuser and have all been described in detail. The propeller test stand is used to acquire propeller thrust as well as mechanical power which is described as well as other approaches to document propeller performance.

## NOMENCLATURE

*CFD* = Computational Fluid Dynamics

*cfm* = cubic feet per minute

*D* = diameter

$\mathcal{E}$  = percent error

*ft* = feet

fph = feet per hour

*g* = gravity

*h* = height

*J* = advance ratio

*M* = Mach number

*mph* = miles per hour

*n* = rotational speed

$\dot{m}$  = mass flow rate

*P* = pressure

$\rho$  = density

*SST* = Shear Stress Transport

*T* = Thrust

$u_{analytical}$  = analytical value

$u_c$  = calculated value

*v* = velocity

*VDC* = volts direct current

*2-D* = Two dimensional

*3-D* = Three dimensional

## CHAPTER

### I. INTRODUCTION

**T**HE development of the large-scale low speed wind tunnel is currently underway at the University of North Dakota (UND). The primary intention of the project is to investigate the losses within rotors and propellers that can be applied to different Unmanned Aerial Vehicles (UAV). This wind tunnel is expected to be a multiuse facility which can be used for a range of experimental investigations. These purposes can include investigating the drag and downforce aerodynamics of UND's Formula SAE car team, testing a small-scale wind turbine, and testing the aerodynamics of UAV's and other aerodynamic models. Conducting inlet and exit surveys to validate the performance of the with tunnel. The facility is located east of Mill Road within the old Minnkota powerplant which is now the UND Drill Lab and Research Facility.

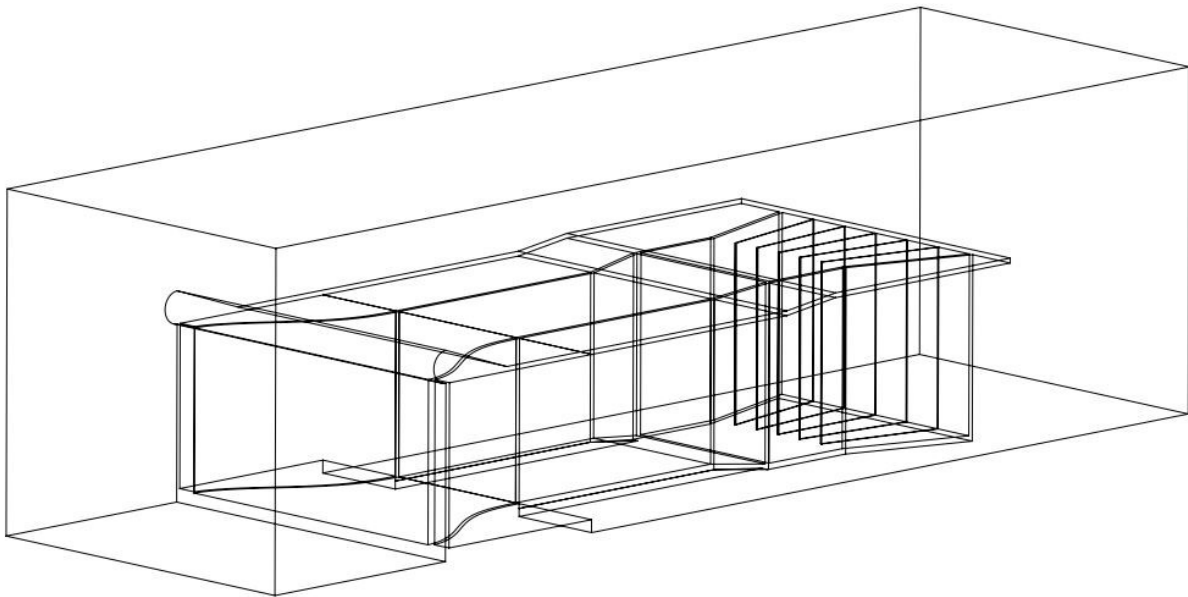


**Figure 1. Wireframe Isometric View of Wind Tunnel Geometry**

Figure 1 shown above represents that of a digital rendering with wireframe view of the entire wind tunnel. This is an accurate representation of the real-world model. From left to right, the inlet contraction flows into the test section leading into the multi-vane diffuser on the far right. Figure

1 shows the entire wind tunnel design where as a picture would only capture sections due to the size of the facility. The wind tunnel occupies about 1700 square feet and the structure is approximately 46 feet in length with a test section of 10 feet by 10 feet spanning 16 feet. The wind tunnel is primarily constructed from wood framing, plywood, and OSB sheets. Acrylic glass has been used for windows located on either side and above the test section for visualization. Although located within a building, walls will be constructed in the future to partition off the wind tunnel section to create a closed loop wind tunnel. Test section velocities up to 30 miles per hour are expected to be generated.

#### **a. Objectives**

The primary objectives of this thesis work are to document the design, construction, and functionality of the completed wind tunnel. The design has been supported by both extensive knowledge of fluid mechanics and scholarly articles described in Chapter II. Construction of the wind tunnel has been completed to an initial functional state and includes every major component of the wind tunnel. Further work must be performed in the future to generate ideal flow conditions. Current progress on the validation of the wind tunnel is dependent upon the completion of the initial functional state wind tunnel as well as the test cart and propeller test stand. The wind tunnel consists of flow conditioning, inlet contraction section, a test section, the axial fans, and a multi-vane diffuser section. Chapter III outlines the construction of these components. The flow conditioning is composed of two sections the flow straightener and fine screen mesh which eliminate turbulence both of which have been constructed. The inlet contraction section is used to accelerate the flow entering the test section and is complete. The 10 feet by 10 feet test section is designed to accommodate scaled propellers and rotors up 40 inches in diameter. It will include inlet and exit surveying capabilities, visual access through the acrylic windows, measurement of test vehicle lift, drag, and downforce, and experimental determination of propeller/rotor



performance. Currently, the drag and downforce cart and traversing sections are under construction. The four 60-inch fans are currently operational. The exit diffuser is largely complete, but some minor enhancements are planned to improve pressure recovery. Partitioning off the wind tunnel facility from the remainder of the building and improving the exit to inlet flow aerodynamics is expected to begin in the near future. A CFD model of the wind tunnel and return flow path has been developed and will be used to improve the recirculation of flow around the wind tunnel which has been discussed in Chapter IV.

A propeller test stand has been purchased from Tyto Robotics which will enable the testing of various propeller and motor configurations. The test stand will allow for testing of single rotor tests up to 25 kg thrust while measuring thrust, torque, RPM, power, motor efficiency and propeller efficiency. An open-source data acquisition software is available from Tyto Robotics that allows for custom written scripts to perform automatic testing. This software will help assist in initial testing phases. Funding from Catto Propellers through a NAVY STTR contract has assisted in the development of this facility. Future work will be conducted in line with the NAVY's research interests of UAV's [1].

## II. BACKGROUND

The background chapter discusses archival literature on the different components within the wind tunnel, CFD turbulence model equations, and propeller testing. The advantages and disadvantages between open and closed-circuit wind tunnels are explained. Research has been reviewed within the inlet configuration detailing both the flow conditioning and contraction ratio. Within the test section literature summarizes that the entire design of the wind tunnel is dependent upon the desired size of test section. The multi-vane diffuser approach for designing an ideal geometry has been detailed to eliminate flow losses and ensure uniformity. Knowledge regarding turbulence modeling has been explained which outlines different turbulence model equations and how they perform in complex flow environments. Archival literature discussing propeller testing, applications of propeller testing slipstream effects and the complex problem of UAVs in descent are also presented.

### *Wind Tunnel Components*

The facility will be operated as a closed loop so achieving a uniform, swirl free, quiescent flow is challenging. Closed-circuit wind tunnels are often more expensive to construct and difficult to design than that of open-circuit wind tunnels [2,3]. Wind tunnels can also be either open jet or enclosed. An open jet test section has no surrounding boundaries and is open to the surrounding air. A closed jet test section is used for this work where the flow moves through a closed region with surrounding boundaries [4]. Closed-circuit wind tunnels have a better flow and lower power factor than open-circuit mainly because most open-circuit wind tunnels are small and operate without exit diffusers. The disturbed air within a closed-circuit is more prominent to that of a closed-circuit wind tunnel because of the recirculation of air [5]. High turbulent energy levels are

expected at low flow speeds which impact the flow quality. The intensity of turbulence has to be reduced before the test section to provide the best conditions for experimentation [6].

The inlet flow straightener and screen are used to reduce inlet swirl which can arise from the flow moving around the turns. They also offer a uniform resistance to the flow that helps to reduce nonuniformities at the inlet. In addition, screens contribute to the suppression of boundary layer separation. The effects of turbulence for a screen can be characterized by the Reynolds number and wire diameter. The mesh size for a supercritical screen should be based upon the length scale of the turbulence generated by the screen is less than that of the incoming turbulence [7]. Trade-offs are often presented when determining the ideal contraction ratio and contraction length. Due to common building constraints for each project, the ideal ratio between each must be determined to achieve the desired flow conditions. Separation of the flow can occur if the contraction is too short for the amount of area reduction [8]. The length of the contraction ratio should be sufficiently small to minimize the boundary layer growth and cost but remain long enough to prevent the development of large adverse pressure gradients near the wall [9]. By developing an analytical analysis of matched polynomials, one can determine the desired shape of the contraction. With specified heights on either end of the contraction and determined distance of intersection, the polynomials can be aligned with respect to their slope and curvature. On either end of the contraction shape, the polynomials can be adjusted to have a slope of zero allowing for a smooth transition of the curve with desired contraction. Computational fluid dynamics (CFD) is commonly used to develop modern profiles, but this allows for a simple analytical approach [10]. Thesis work developed by Healzer, Moffat, and Kays assisted in developing the contraction shape used [11].

The flow within the test section is typically dependent upon the requirements of the experiment. Cost and power are directly determined by the cross-sectional area. Differences in losses of the

test section due to shape are negligible. Therefore, the shape of the test section should be dependent upon the use and aerodynamics considerations. When exiting the inlet contraction, flow takes about 0.5 diameters before the flow reaches an acceptable level of uniformity [2,12].

The purpose of the diffuser allows for the deceleration of the test section velocity and converts the dynamic pressure into static pressure essentially recovering the pressure in a relatively compact distance. Two-dimensional diffusers have been widely used for their simplicity in geometrical changes. The use of a multi-vane diffuser enhances uniformity of the flow and can recover up to 90 % of the dynamic pressure. Too abrupt of the angle of the diffuser can result in different types of stalls including large transitory stall, stall off one surface, and even jet flow. Also, flow visualization is easy to apply and assists in identifying and avoiding regions of flow separation [13]. The use of a wide-angle diffuser may result in separated flow along the wall and create significant losses. The performance of the diffuser is dependent upon the Reynolds number, velocity distribution, turbulence intensity, divergence angle, area-ratio, and diffuser length. With the addition of splitter vanes, the recovery of pressure proves to be greater while also creating a more uniform velocity distribution in a much more compact distance and preventing incipient separation [14]. Often, screens placed before the diffuser are used to correct nonuniform velocities. Screens generate significant pressure losses at higher velocities and therefore create greater power losses. [15-17].

### *CFD Turbulence Models*

With the advancements in computers in recent decades, the use of CFD has proven to be a useful tool in the design and evaluation of fluid systems and heat transfer. Although extremely useful, several complications may arise when developing analyses. An extensive background in fluid mechanics and heat transfer is required when performing an analysis to ensure computed

results match that of expected outcomes. Two equation turbulence models are most often selected for engineering computations due to their computational efficiency, reasonably accurate estimates of eddy viscosity and well-known problems. The major problem with two-equation models within CFD is their failure to correctly predict the onset and amount of separation in adverse pressure gradients. Aerodynamics research is poised between experimental and computation techniques. The two are directly related and as progress develops within numerical methods and advanced CFD models, more advanced experimental data is required for validation [18]. The only method to establish validity of theoretical arguments is to test the resulting model against several challenging and well documented research flows. Accurate theoretical predictions of flow performance require that the turbulent boundary layer be correctly described [19]. These include the adverse pressure gradient test which includes a flat plate with a wall parallel that begins to diverge. This induces an extreme adverse pressure gradient. Another challenging research flow is that of the backward facing step. In this flow, uniform flow flows past a 90-degree downward step inducing separation and turbulence in the stagnation region. Accurately predicting flow fields can be accredited towards both turbulence modelers and advancements in numerical methods [20,21]. The  $k-\omega$  model is the model of choice within the sublayer and log-law regions of the boundary layer. Unlike other two-equation models, the  $k-\omega$  model does not involve damping functions. Due to its simplicity, the  $k-\omega$  model is superior to other models, especially in regard to numerical stability. One disadvantage of the  $k-\omega$  model like many turbulence models is the inability to correctly predict the behavior of the turbulence as it approaches a wall. In addition, the  $k-\omega$  model does not accurately represent the  $k-\epsilon$  distribution in agreement with the direct numerical simulations (DNS). DNS with regards to CFD meaning the computation of flow using the Navier-Stokes equations without any turbulence model. In the wake region of the boundary layer, the  $k-\epsilon$

model favors the  $k-\omega$ . Although the behavior of model in the logarithmic region is of importance, it is the level of the eddy viscosity in the wake region that ultimately determines the ability of an eddy viscosity model to accurately predict strong adverse pressure gradient flows. The development of a new model called the Shear Stress Transport (SST) includes the original  $k-\omega$  model in the sublayer and log-law regions which then transitions to the standard  $k-\epsilon$  model in the wake region of the boundary region. The SST model leads to significantly improved results for flows experiencing adverse pressure gradients. The developed model requires an increased amount of computation time, but more importantly has proven stability in complex applications [20]. The SST turbulence model has since been widely used and proven to be a reliable model performing under several types of flows. The most updated model since its development only has changed two terms within the equation [22].

### *Propeller Testing*

The UAV industry has rapidly gained interest over the years and with that so have the propellers that power the vehicles. Deters, Ananda, and Selig state that performance terms of power and thrust are used to describe propellers but more research is required to farther examine the effects of the produced slipstream. The impacts for the slipstream result in trailing wake that may lead to disturbance in flight during formation or swarm operation. The thrust divided by the propeller disk area is called the disk loading which is an important factor. An increase in the disk loading will increase the induced velocity. This concept can be used as an explanation of how the Reynolds number affects the slipstream of a propeller. The Reynolds number also impacts the thrust coefficient of a propeller which directly impacts the produced thrust. Along with this, smaller UAV's due to size and weight are susceptible to gusts [23]. Large vortices are formed around the edge of the rotor through the interaction of the induced flow from the propeller and the descent.

This is known as the vortex ring state (VRS) which can be observed when the descent velocity has similar magnitude to that of the induced velocity [24]. The momentum theory is a common method applied when a measurable slipstream is created. In the momentum theory, the propeller is assumed to be an actuator disk with a discontinuous increase in static pressure. With the absence of a defined slipstream during the VRS phenomenon the momentum theory is impractical therefore, considerable research was conducted to better understand the phenomena. Figure 2 represents how the flow around a propeller is modeled [23].

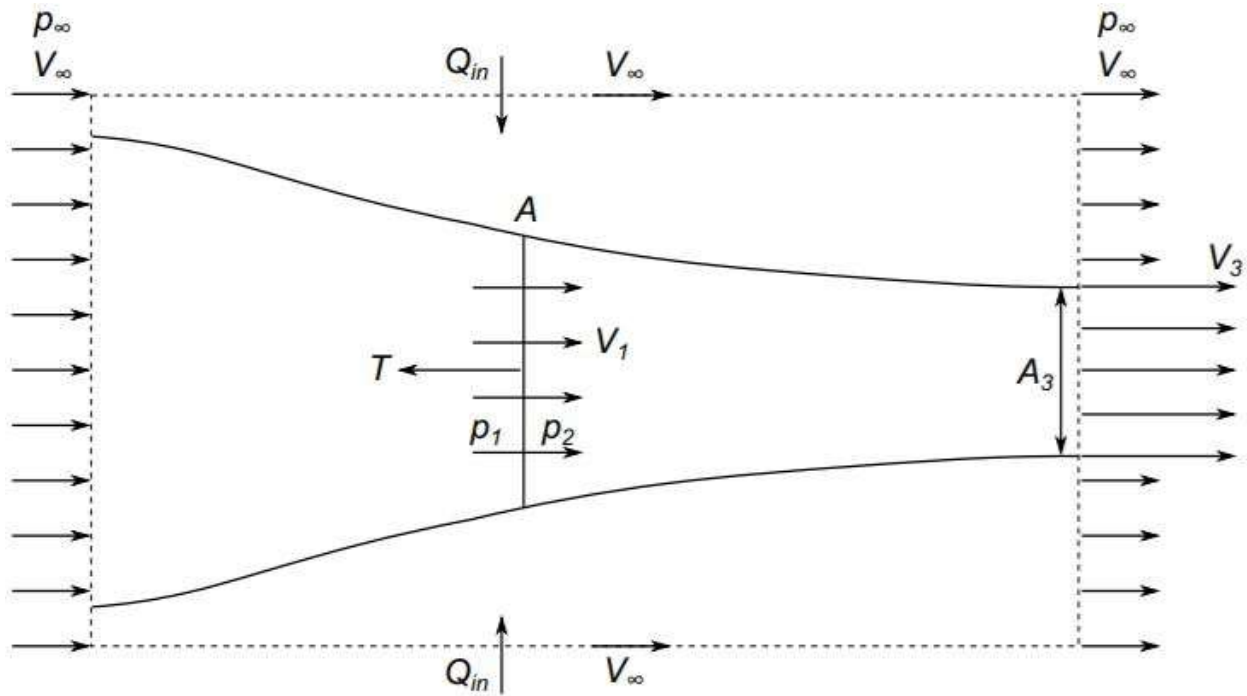


Figure 2. Flow around a Propeller using Momentum Theory

The archival literature discussed supports the design, construction, and validation of the wind tunnel. This literature guided the design of the flow conditioning, inlet contraction, test section, test cart, propeller test stand, traversing section, fan assembly, and multi-vane diffuser. The literature also covered the importance of selecting the correct turbulence model to provide sufficient computational results. The last section of propeller testing supports the need for research

within propeller testing as well as methods for achieving results. Following this section, the details of each section are fully described and outline the approaches taken as well as the obtained results and expected results.



### III. EXPERIMENTAL AND COMPUTATIONAL APPROACH

Within Chapter III, the analytical solutions, CFD simulation setup and approach, and wind tunnel components are explained. The mass flow rate produced by the fans guides the sizing of both the inlet contraction and test section. The CFD simulation geometry development, boundary conditions, and use of a mesh interdependence study are used to ensure produced results have confidence. Within the last section, the design and construction of the flow conditioning, inlet contraction, test section, test cart, propeller test stand, traversing section, fan assembly, and multi-vane diffuser are explained with figures documenting the progress.

#### a. Analytical Development

##### i. Fan Mass Flow Rate

In this section the volumetric flow rate of the fans is used to estimate velocities through the test section and other components as well as estimates of the pressure drop in the flow conditioning are also outlined. Each fan within the assembly had a manufacturing specification of 66,000 cfm. With four in total, this equates to 264,000 cfm flowing through the fans. With the diameter of each fan equating to 60 in, the computed cross-sectional area of air flowing through the fans equals 78.54 ft<sup>2</sup>. With the use of Bernoulli's equation listed in Eq. (1), the method of developing the flow within the test section can be calculated due to the wind tunnel essentially being a closed duct. Being incompressible flow, the density is held constant and the test section cross sectional area of 100 ft<sup>2</sup> is used for the calculation. A simple conversion from cfm to mph is completed. 264,000 cfm divided by the test section cross sectional area of 100 ft<sup>2</sup> results in 2640 fpm. By multiply this value by 60 minutes, the minutes are converted to hours which results in 158,400 fph. Finally, converting the feet to miles can be done by dividing the previous value by 5280 ft/mile. The effects of the potential energy terms can be neglected when working through Eq. (1) [25]. The

primary assumption of this analysis is there is no leakage through the wind tunnel. With the primary material of wood being used during construction, any holes that exist may easily be patched. The computed velocity through the test section of the wind tunnel is commuted to a value of 13.48 m/s or approximately 30.15 mph.

$$P_1 + \rho gh_1 + \frac{1}{2}\rho v_1^2 = P_2 + \rho gh_2 + \frac{1}{2}\rho v_2^2 \quad (1)$$

### ii. Subsonic Nozzle Contraction

Equation (2) for quasi one-dimensional incompressible flow with constant density through a varying area duct states that according to the conservation of mass the derived continuity equation of mass flow is constant [26]. Assuming constant density, the relationship between area and velocity is formed. The area ratio between the beginning of the inlet contraction and test section cross-sectional area is 2:1. The initial velocity entering the inlet contraction equates to approximately 15 mph.

$$\dot{m} = \rho VA = \rho_1 A_1 v_1 = \rho_2 A_2 v_2 \quad (2)$$

### iii. Flow Conditioning

The construction of the flow straightener was performed using hardboard sheets with a 1/8<sup>th</sup> inch thickness. These were assembled in a grid matrix which was meshed with one another to achieve a desired uniform grid. Exact dimensions of the flow straightener hardboard sheets were used to determine the pressure drop and blockage across assuming 15 mph. The total cross-sectional area of the inlet is subtracted from the wetted cross-sectional area created from the hardboard sheets. This creates a total area of blockage through the flow straightener of approximately 2.13 m<sup>2</sup>. With this blockage, the area is reduced and the velocity speeds up to a value of roughly 17 mph. Assuming a density of 1.16 kg/m<sup>3</sup>, the dynamic pressure is computed to

a value of 32.27 Pa using Bernoulli's relationship. To solve for the expected drag acting upon the flow straightener, a coefficient of drag equal to 2 is assumed. Often flow over a flat plate has a coefficient of drag greater than 1. With the added constructed assembly being imperfect this value will be well over 1. The computed value of drag results in 142 N of force acting upon the flow straightener. The drag divided by the total cross-sectional area results in a pressure drop of 7.62 Pa. The Reynolds number was computed for an individual cell at 48087. This was used to determine the drag force created from the boundary layer. The total length of each of the cells wetted perimeters was determined and summed together. The drag coefficient from the computed boundary layers was multiplied by the total wetted perimeter to solve for the boundary layer induced drag of 29.5 N. The total drag force acting upon the flow straightener summed to be approximately 171.5 N. This final computed drag was then used to estimate the total pressure drop across the flow straightener with a value of 9.21 Pa.

The total pressure drop across the fine mesh screen can be estimated similarly. Assuming a spacing between each wire of 0.12 inches and a turbulence of 8 % leaving the fine mesh screen, the pressure drop of 14.66 Pa is computed. Summing the pressure drop across both the flow straightener and fine mesh screen, the total pressure drop across the flow conditioning is 23.88 Pa. The dynamic pressure at the start of the flow conditioning is 104.31 Pa assuming the inlet flow being 15 mph with the same density stated earlier. The dynamic pressure of the fans is solved using the expected velocity output from the manual. The computed dynamic pressure is approximately 158.39 Pa. The difference in pressure between the start of the flow conditioning and the output of fans has over a 50 Pa change. Ensuring proper sealing and contouring of the exit fan profile will help recover pressure and improve performance during operation.

## **b. CFD Simulation Setup**

### **i. Geometry**

The CFD simulation was conducted with the use of ANSYS CFX. The fluid domain represents that of the real-world facility with a few assumptions to the design. The CFD simulation is utilized to better understand the effects of the 180° turns and expected losses in flow occurring. The total length of the wind tunnel is 46 feet 4 inches. The inlet curved “S” profile has been constructed. The inlet has a contraction area ratio of 2:1. This allows for the velocity to accelerate to a value of 2 times the entering flow. The initial dimensions at the inlet are 20 feet wide and 10 feet in height. The inlet contracts in width to a minimum dimension of 10 feet wide. The inlet contraction spans over 12 feet. Throughout the inlet and test section the height remains constant at a value of 10 feet. With cross sectional dimensions of 10 feet wide and 10 feet in height, the test section spans a total length of 16 feet. Preceding the test section, the fan assembly follows which expands to a cross section of 11 feet wide and 11 feet in height. This symmetrical transition occurs over 4 feet which allows for a smooth transition into the fans. The actual fans are mounted at the end of this structure. Four fans are constructed together all composed of a square geometry with a dimension of 66 inches on every side of the fan. Following the slight expansion to the fan assembly, a constant cross section is maintained until the diffuser. This cross-sectional area has dimensions of 11 feet wide by 11 feet in height. This spans over the length of 6 feet. The diffuser section expands to a maximum cross section of 16 feet wide by 11 feet in height. Within the diffuser, five vanes are inserted proportionally throughout and extend through the entire length of the diffuser of 8 feet. The roof of the wind tunnel expands the entirety of the width of the room of 23 feet and extends the entire length of the geometry. Figures 3 and 4 shown below represent the 2-D profile of the geometry created from a side and top view.

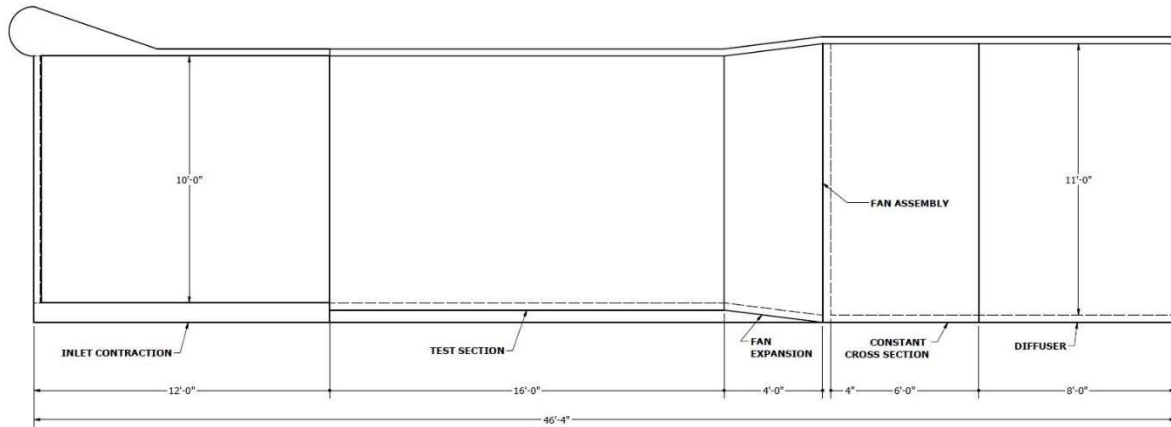


**Figure 3. CFD Geometry 2-D Side View**

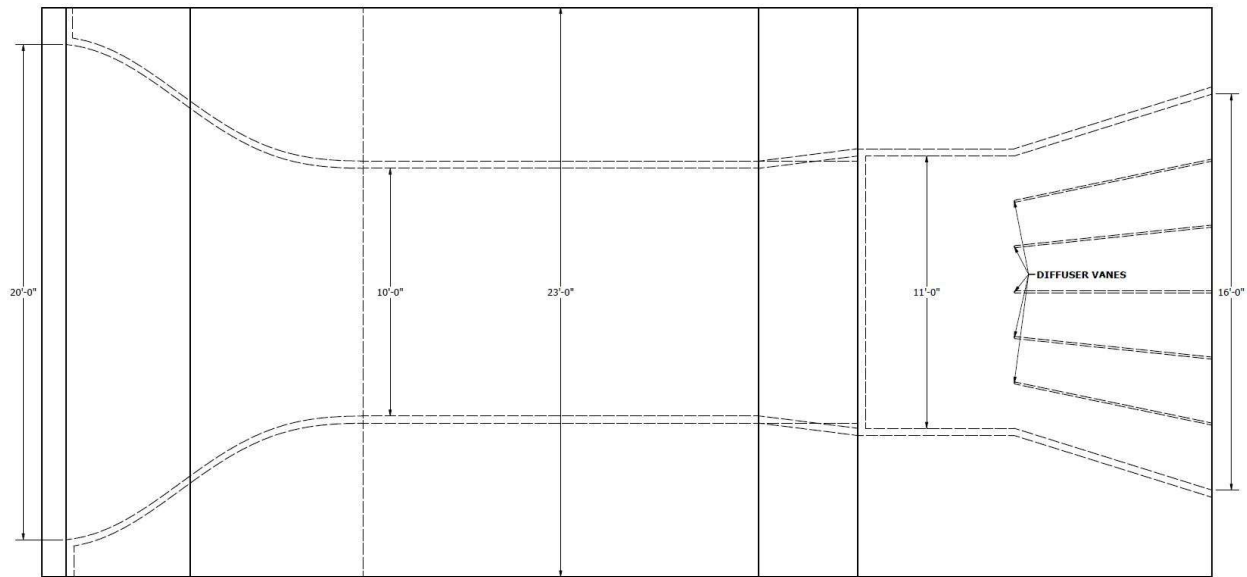


**Figure 4. CFD Geometry 2-D Top View**

The geometry was primarily developed with the use of Autodesk Inventor. The addition of a curved inlet top was added to achieve better flow around the top side of the inlet and reduce separation. In order to simulate flow within the tunnel, the fan assembly at the aft side of the test section was modeled as a solid extrusion of 4 inches in depth. This allowed for boundary conditions to be stated on each side of the extrusion. Once completed, the CAD model was exported as a Parasolid file into Solidworks. Once imported into Solidworks, the addition of the room volume

was added to create the fluid domain. The width of the room volume was set as 23 ft. with a height of 21 ft. The length of the total room volume was 76 ft. with the front of the extruded volume extended 14 ft. from the start of the inlet contraction. This correlates with the building constraints for which the wind tunnel is currently being developed. A Boolean operation was performed that subtracted the wind tunnel geometry from the room volume. The result was a single geometry that contained the entirety of the fluid domain. This geometry was exported as a .IGES file to be imported into ANSYS Workbench Design Modeler to begin CFD preparations within the CFX software. Figure 5 seen below represents an isometric view of the 3-D wireframe geometry.

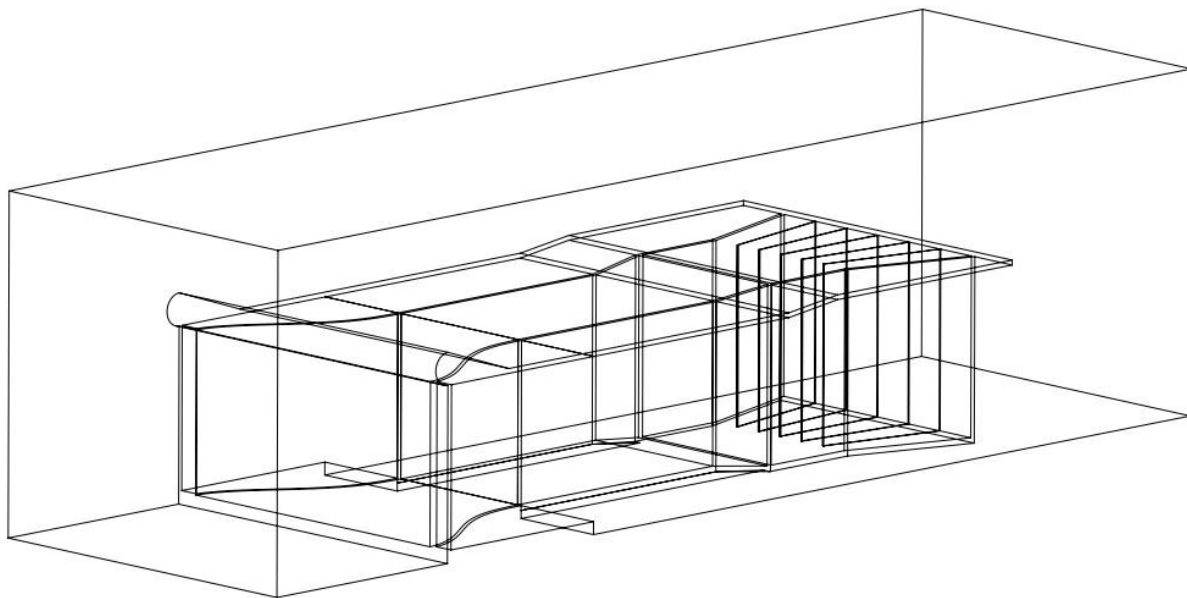


**Figure 5. Wireframe Isometric View of Wind Tunnel Geometry**

## **ii. Boundary Conditions**

The fully developed flow within the test section is computed to be approximately 13.48 m/s. The calculated values of pressure and velocity were used to guide the simulation analysis. The flow conditions set within the CFX solver were a velocity inlet at the exit of the fans at 13 m/s or approximately  $M = 0.04$  therefore incompressible. The velocity created from the fans was assumed to be turbulent, so a high turbulence intensity setting was used of 10 %. With the assumption of

sea level atmospheric conditions of single-phase flow, the density was set to 1.225 kg/m<sup>3</sup> and the dynamic viscosity set to 1.789E-05 kg/m/s. As stated above, the velocity inlet will be set at the exit from the fans. This in turn will create flow circulating over the top into the inlet contraction. A pressure vented outlet is set to the front of the fans to allow for the induced velocity to exit. This pressure is set to 101325 Pa atmospheric conditions. The no-slip wall boundary condition will be applied to the entirety of the remaining geometry to simulate the near wall effects of shear stress. The turbulence model used for the analysis is the SST model paired with the k- $\omega$  model due to the amount of research and performed on this model. It is a two-equation partial differential equation model. The analysis is performed at steady state.

### iii. Mesh Interdependence Study

The purpose of the mesh interdependence study was to evaluate the computational costs of each mesh and the accuracy of which each compute. An analytical solution was developed and set to 17.48 m/s to compare the centerline velocity profile within the test section. The centerline profile was specified to be within the middle of the test section and far enough inside to evaluate the maximum velocities. Each mesh developed was compared to achieve a percentage of error between the simulated and analytical computation using equation 3. Listed below are the values set for each mesh developed.

$$\varepsilon = \frac{|u_c - u_{analytical}|}{u_{analytical}} \times 100 \quad (3)$$

The arbitrary mesh consisted of a body sizing on the entirety of the geometry of 0.5 m. With this sizing, the resultant mesh generated 109022 nodes and 73013 elements. Figure 6 shown below represents an isometric view of the developed arbitrary mesh.

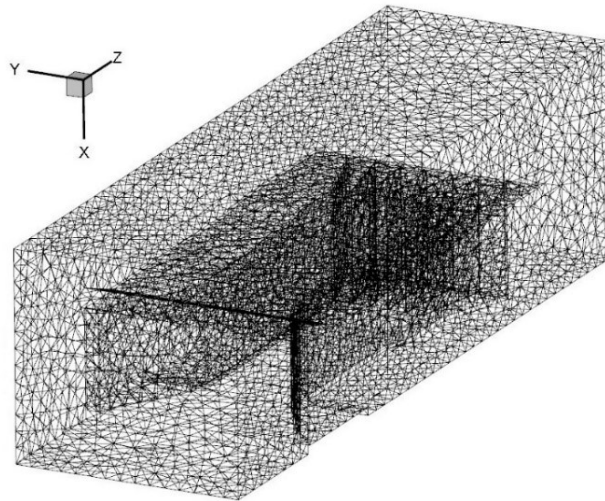


**Figure 6. CFD Geometry Arbitrary Mesh**

The intermediate mesh also consisted of a body sizing on the entirety of the fluid domain. This sizing was set to 0.4 m. The resultant mesh generated 200199 nodes and 137219 elements. Shown below Fig. 7 represents an isometric view of the intermediate mesh.

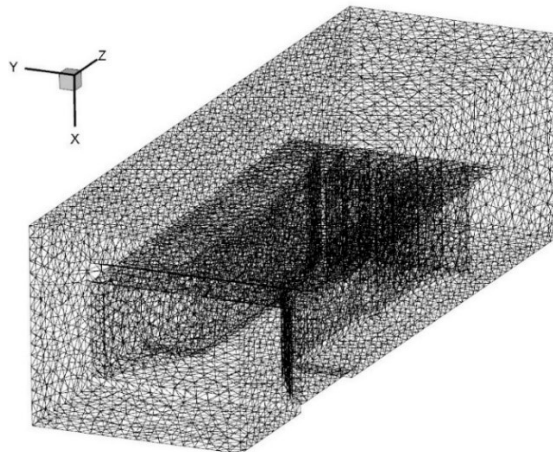


**Figure 7. CFD Geometry Intermediate Mesh**

For the final, fine mesh, the body sizing was also applied to the entirety of the fluid domain. This sizing was the smallest setting at a value of 0.3 m. The resultant mesh generated 462093 nodes and 323285 elements. Figure 8, shown below represents an isometric view of the fine mesh.



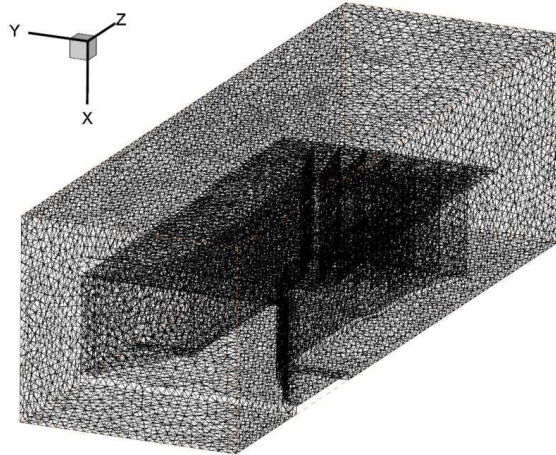


**Figure 8. CFD Geometry Fine Mesh**

To evaluate the accuracy of each mesh, the centerline velocity profile of each was compared against each other. The centerline velocity profile was specified at determined distanced into the test section far enough inside to correctly evaluate the fully developed flow. As stated above, the values from the centerline velocity were compared to that of the analytical analysis to find the percent error between each. Figure 9 and table 1 shown below represent the comparison and percent error between the evaluated meshes. The percentage of error was evaluated at the near wall section approximately 2.25 m. This is due to the fully developed flow effects that each mesh accurately captures near the center.

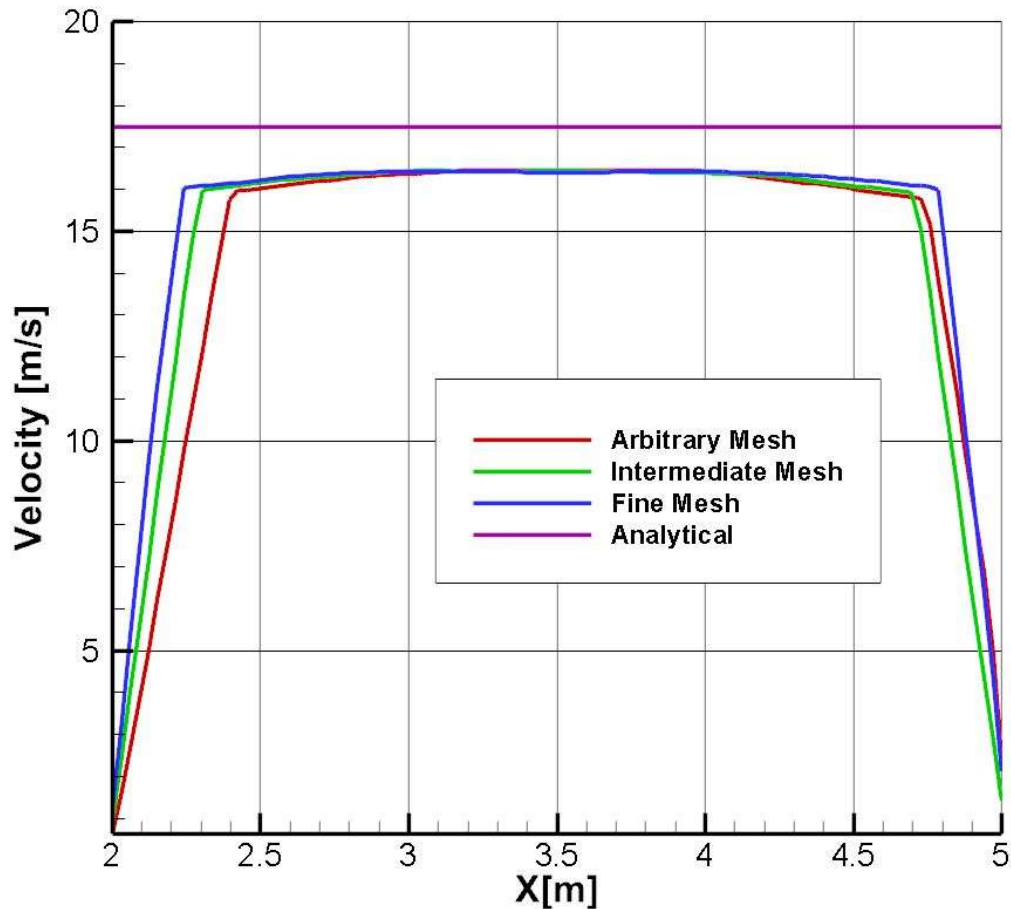


Figure 9. Centerline Velocity Mesh Comparison

Table 1. Centerline Mesh Comparison Percent Error at 2.25 m

Mesh	<i>Arbitrary</i>	<i>Intermediate</i>	<i>Fine</i>
<b>Percent Error</b>	37.34 %	14.64 %	8.14 %

The results from this comparison suggest that the fine mesh provides the most precise analysis. Although each mesh accurately measures the maximum velocity near the center, the fine mesh provides a more refined solution to that of the near wall. The primary assumption within this analysis is the analytical solution was developed with the conservation of mass without turbulent losses whereas the results from computation includes turbulent losses therefore suggesting a decrease in maximum velocity. Due to the shear stress developed from the no-slip condition, the fine mesh accounts for the boundary layer created the best. This can be noted by the percent error

developed from each within Table 1. With this interdependence study, the fine mesh was selected as the optimum mesh and is used for farther analysis within the results.

### **c. Wind Tunnel Components**

This section documents the experimental design of the wind tunnel and its construction. The wind tunnel is currently enclosed in a large room (approximately 23 feet x 21 feet x 76 feet) which is open on one side. The wind tunnel consists of a flow straightener, inlet screen, a 2 to 1 area ratio inlet contraction, a 10 foot by 10 foot by 16 foot long test section, a axial fan array, and a multi-vane diffuser. The inlet flow straightener consists of 7200 2-inch by 2-inch by 4-inch long square flow channels across a 10 foot by 20 foot inlet and is designed to take out the inlet swirl. A fine nylon window screen is placed 18 inches downstream from the flow straightener and is designed to help remove nonuniformities in the flow. The smooth 2 to 1 area ratio contraction accelerates the flow into the test section further improving the flow uniformity. The test section has an inlet area of 10 foot by 10 foot and 16 feet long and includes large windows, doors, an inlet and exit traversing section and lighting. Within the test section, the test cart, propeller test stand, and traversing section are described. Downstream of the test section, the fan assembly is composed of four 60-inch axial Drayton fans mounted in a square assembly of 11 feet by 11 feet. The multi-vane diffuser has five splitter vanes than diffuse from 11 feet by 11 feet to a maximum area of 11 feet by 16 feet which allows the flow to obtain better uniformity while remaining within a compact distance.

#### **i. Flow Conditioning**

The flow conditioning is composed of two main sections. The initial coarse flow straightener, and the fine screen mesh. Combined, both components supplement the wind tunnel by providing uniform low disturbance flow that can accelerate into the test section. Uniform low disturbance

flow within the test section is essential to providing accurate results when testing. The flow straightener eliminates the swirl from large eddies developed from the return flow and provides a uniform resistance that helps to reduce flow nonuniformities. The structure was developed using smooth hardboard material that is approximately 1/8<sup>th</sup> inch in thickness. A goal of 2-inch by 2-inch square grid was desired which spans the entire area of the inlet, a total of 7200 squares. To construct the flow straightener, hardboard sheets with dimensions of 4-feet by 8-feet were set on top of one another and bolted together constrained at every edge. This allowed for quicker manufacturing. With a total of 28 sheets of hardboard, each sheet was then cut lengthwise to produce thin strips each 4 inches in width. Each set of strips was then precisely measured and marked every two inches to begin cutting 2-inch slots. The use of a radial arm table saw assisted in cutting each slot. This process was very tedious and took some time to complete. Due to the blade thickness of the table saw being less than that of the hardboard, two blades were used during the cutting process. A few of the slotted 4-inch strips were cut down to 2 feet to allow for overlap when assembling the grid matrix. To assemble the grid matrix, first a temporary and permanent frame was first developed. The use of 2x4's and 2x6's supplemented this process. A 2x4 wall spanning the area of the whole inlet was created to allow for the matrix to be developed on top of that assembly. The slotted 4-inch strips of 8 feet and 2 feet in length were then used to begin assembling the grid matrix. This process took some time and was tedious during assembly. Figures 10-12 show the grid matrix during this process.



**Figure 10. Flow Straightener Matrix Assembly**



**Figure 11. Mounting of Flow Straightener**





**Figure 12. Completed Flow Straightener**

The design of the fine screen mesh was comprised of window screen, a wooden frame, and steel bars. Due to the area of the inlet, the window screen needed to be sewn together to achieve full coverage. The screen was rolled out across several tables, aligned, and pinned together. The use of a sewing machine allowed for quick stitching. A vertical stitch was sewn and next to that a zig-zag stitch was sewn. The combination of these stitches created a sufficient bond that could not be separated. Figure 13 represents the stitching sewn on the screen.



**Figure 13. Fine Mesh Screen Stitching**

The completed sewn screen was now ready to be mounted to that of the developed wooden frame. The wooden frame for the fine mesh screen was created with 2x4's and 2x6's. The sewn screen was laid out across frame and stretched until taut. The use of staples was used to fix the screen to the wooden frame. Due to the size of the inlet being 10 feet by 20 feet, the fine mesh screen would experience significant deflection during operation. To prevent this, the use of 2 steel bars was used at each seam. These bars measured  $\frac{1}{4}$  inch by  $\frac{3}{4}$  inch. They were cut to 10 feet and aligned vertically with the two seams created. A 2-step epoxy was used to bond the seams of the screen to that of the steel bar. 90-degree brackets were mounted on both the top and bottom of the steel bar to constrain it to the wind tunnel's structure. After fully assembled, the fine mesh screen was securely mounted to the inlet of the wind tunnel with minimal deflection. Figure 14 shown below represents the fully mounted fine screen mesh.



**Figure 14. Fine Mesh Screen Mounted**

## **ii. Inlet Contraction**

The inlet contraction has a total contraction ratio of 2:1 as stated earlier. With an initial cross-sectional area of 200 ft<sup>2</sup> and contracting to the test section area of 100 ft<sup>2</sup>. The total length of the inlet contraction spans 12 feet. To develop the “S” shape curve an assumption was made that the distance between each point was a straight line rather than the curve shown in figure 15 below [27].



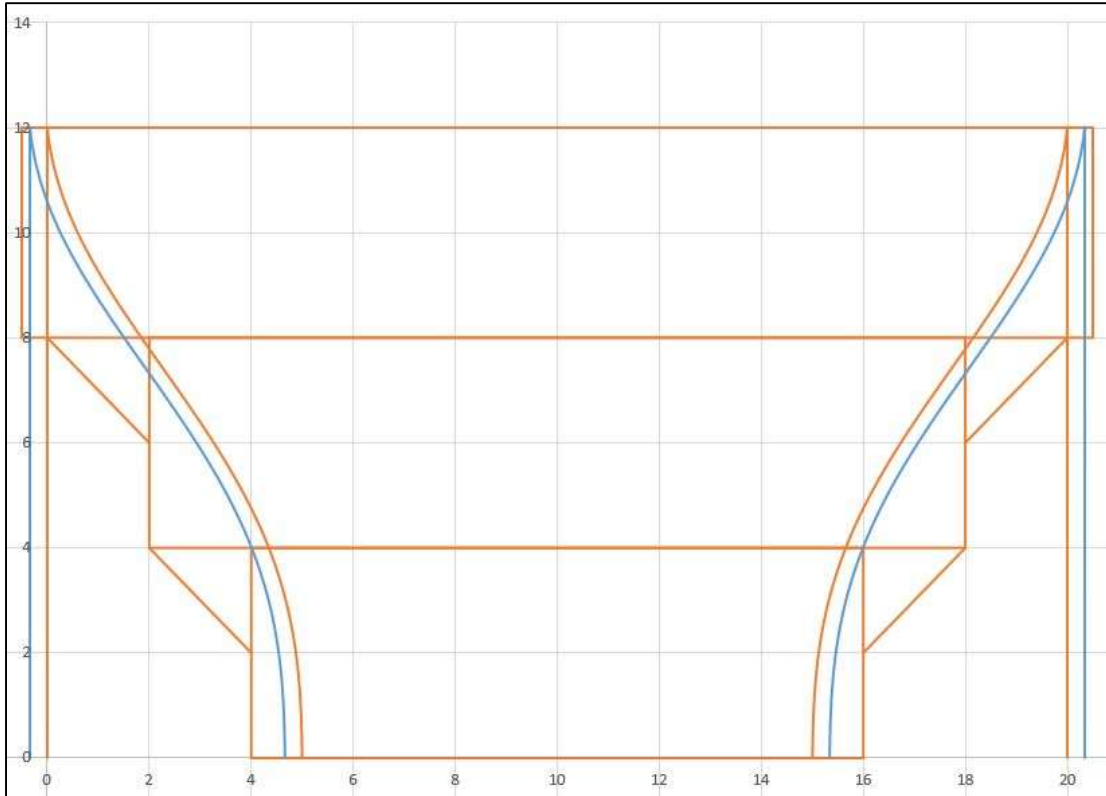


**Figure 15. Inlet Nozzle Base Curve**

This allowed for the total distance of the curve to be easily calculated using equation 4-6 where “X” is the distance along the centerline of the curve and x and y are the coordinates used during assembly. Results in excel are tabulated within Appendix A. These dimensions were used during the assembly of the inlet contraction to constrain each curve.

$$F(X) = X^4(15 - 24X + 10X^2) \quad \text{Eq. (4)}$$

$$x = \frac{X \text{ (in)}}{144} \quad \text{Eq. (5)}$$

$$y = 60 + F(X) \times 60 \quad \text{Eq. (6)}$$

The floor and ceiling of the inlet were created using 2x4’s and 2x6’s. A supporting wall was developed on one side of the wind tunnel to allow for the ceiling to be supported. The other side

of the wind tunnel contained an I-beam from the original building that ran length wise of the wind tunnel. This was used as the other support of the ceiling of the wind tunnel inlet contraction. Due to the width of the inlet spanning 20 feet, 2x6's were used and spliced together to create a supporting beam that would span to both sides of the inlet contraction. Smooth plywood sheets were used to create an ideal surface for both the floor and ceiling. The plywood on the ceiling and the particle board mounted on the top helped to substantially stiffen the span. The "S" shape curve on either side of the inlet was developed using 2x4's and lauan plywood. Initially, a frame was developed to allow for the construction of the lauan plywood. By laying the frame on the floor, the lauan plywood was fastened on top. The frame and constructed lauan sheets were raised vertically and the lengthwise 2x4's constraining the frame were removed. This allowed the wall to bend freely lengthwise. The vertical 2x4's supporting the lauan sheets were constrained using 3-inch wood triangles that had been ripped with a table saw in the diagonal direction. This allowed for the inlet wall to be fixed to the floor and ceiling. These were uses on either side of each 2x4. The entire inlet was painted black to aid in visualization of the flow during operation. Below, Fig. 16 and 17 represent the 3-D model of the inlet assembly with 2x4's and the constructed inlet.

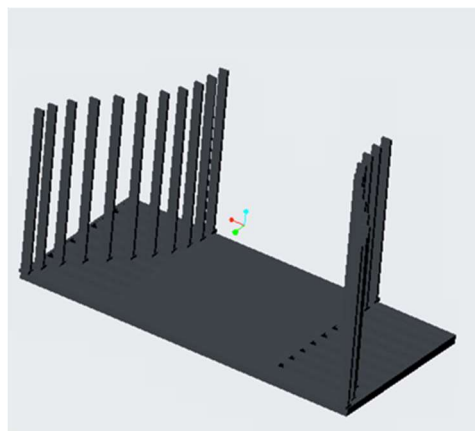


**Figure 16. Inlet Contraction 3-D Model**



**Figure 17. Constructed Inlet Contraction**

### **iii. Test Section**

The test section has dimensions of 10 feet wide and 10 feet in height. This constant cross-sectional area of 100 ft<sup>2</sup> spanned the length of 16 feet. Within the test section, acrylic glass was utilized on both sides of the test section as well as the ceiling. This allows for visualization of the flow phenomena. Traversing section channels were developed within the ceiling. This opening will allow for the assembled traversing section to move laterally back and forth. Due to expected losses from the opening, brushes were used and mounted in the open channel to ensure the air flow would be guided past these sections. Two traversing section channels were created. One fore at about 1 foot 9 inches and one aft of the middle of the test section at 14 foot 3 inches approximately. During testing, these traversing sections can provide essential information on inlet flow uniformity as well as the post model flow. The floor of the test section was constructed using smooth plywood

sheets and 2x4's and 2x6's. An opening was developed in the exact center of the test section with dimensions of 5 feet by 7 feet. This will allow the test cart to be added to measure downforce, drag or thrust loads occurring during testing. Doors on either side of the test section have been added to allow access to the tunnel for model access and setup. Some of the components being tested are large, therefore double doors were created from the control room into the test section. The formula SAE car team on campus provided the width of their vehicle and this guided the design of the double doors and the downforce cart. A removable middle support of the double doors was essential to ensure the vehicle could be placed within the test section when needed. Fluorescent lighting was mounted on the ceiling to illuminate the test section during operation. Alongside of the test section, a small control room was constructed to allow for personnel to observe and perform work on computers during testing shown below in Fig. 18.



**Figure 18. Test Section Control Room**

Wiring from the test cart and propeller test stand will be routed through conduit inside the control room into the data acquisition unit. The data acquisition unit is a HP3497a with an integral voltmeter with 100 channels of input and a 1 microvolt resolution. It runs on an IEEE488 bus which is a method of communication with computers developed years ago. The test section was also painted black like the inlet to aid in visualization during operation. Figure 19 below shows the constructed test section.



**Figure 19. Constructed Test Section**

#### **iv. Test Cart**

The test cart has load cells to acquire measurements of thrust, drag, and downforce. The test cart has dimensions of 5-feet by 7-feet and has been primarily constructed with 2x6's and laser cut 1/8-inch steel. Steel swing arms extend from each wheel assembly to the top center of the frame. A vertical spring has been mounted on the top of each wheel assembly to the top of the frame. Four load cells were mounted at the location of each vertical spring. The wood pieces were constructed to be the frame which outline the perimeter of the test cart and offer structural support across the whole platform. Notches were cut fore and aft of the test cart wooden frame with a metal plate mounted on the top of the frame. The load cells were mounted within this area to measure both thrust and drag. Inline skate wheels were grouped together in an assembly with Annular Bearing Engineering Committee rating 9 (ABEC 9) bearings. The bearings and wheels are already designed to support the weight of the adult user when roller skating. Because of this, the wheels operation during dynamic loadings will be robust enough for this application [27]. The steel sheet metal was



bent into place and welded together to create a robust base. On top of the metal base, the wooden frame rests. At every corner, the height may be changed by turning the adjustable foot. This will allow for the smooth transition from the test section to the test cart during operation. A  $\frac{3}{4}$  inch plywood sheet will be mounted on the top of the entire test cart to serve as the platform for conducting tests. In the future, the idea of having a hinged top plywood sheet as been discussed to allow for access into the test cart mechanics. This would enable to user to easily perform maintenance within the test cart assembly. Signal and power wiring have been routed through the test cart and conduit has been placed from the test cart hole within the test section to the control room. A 24 VDC 40 amp power supply has been mounted on the test cart. This will enable the propeller test stand to have quick access to power as needed. Figures 20 and 21 represent that of the CAD drawing of the proposed test cart design and the developed model in real life.

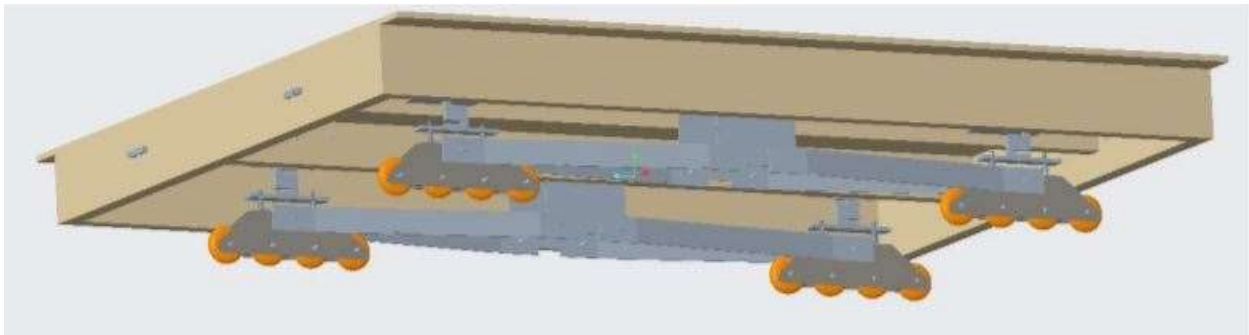


**Figure 20. Test Cart CAD Model**



**Figure 21. Constructed Test Cart without Plywood Top Sheet**

#### **v. Propeller Test Stand**

The propeller test stand was purchased from Tyto Robotics. The configuration used is the Series 1780 Test Stand: Single motor with a 25 kgf 100-amp dynamometer. This propeller test stand will be used with one motor to characterize larger UAV propellers. The 1780 test stand allows for the voltage, current, thrust, torque, and RPM to be measured live [28]. The 1780 test stand can also be converted to a coaxial version with added purchase. Within the 1780 test stand kit the following was included: 25 kgf dynamometer, mono main board V2, main board power adapter, power and control console 100-amp, fixture brackets and fasteners, support plates, motor mount, and mechanical safety stop. Along with the 1780 test stand, the 1585 dynamometer from Tyto Robotics was also purchased. This dynamometer can measure 5 kgf 55-amp. With both dynamometers,



different diameters of propellers can be tested while remaining within the measurements range of accuracy. In addition to the above stated components, the following accessories were also purchased: ground railing system, no-solder board, 3 temperature probes, pressure probe, optical RPM probe, and airspeed probe. With these components, both the 1780 and 1585 test stands can both be operated. The user may specify a range of assorted motors and propellers for testing due to the versatility propeller test stand. The ground railing system allows for the propeller test stand to slide laterally as needed. Eight mounting brackets are attached to every side of the ground railing system to fix the system into the ground. The propeller test stand will be bolted into the plywood sheet of the test cart with the use of threaded inserts that will be glued. This will enable the quick assembly and disassembly of the propeller test stand within the wind tunnel as well as permanent connections into the test cart without potentially cross threading the mounting bolts. Also, with the expected testing of different components aside from propellers, this will keep the setup time minimal. With the power supply mounted within the test cart assembly, an electronic speed controller (ESC) of choice may be mounted on the propeller test stand that is suited for the motor. The no-solder board allows for quick connections between that of the power supply to the ESC to the motor. The mono main board V2 serves as the common terminal for all measurement probes. A USB cable directly connects to the mono main board V2 which will be routed into the control room for data acquisition. Figure 22 and 23 shown below represents the CAD render of the 1780 test stand in the single motor configuration as well as the current assembly of the Series 1780 Test Stand.

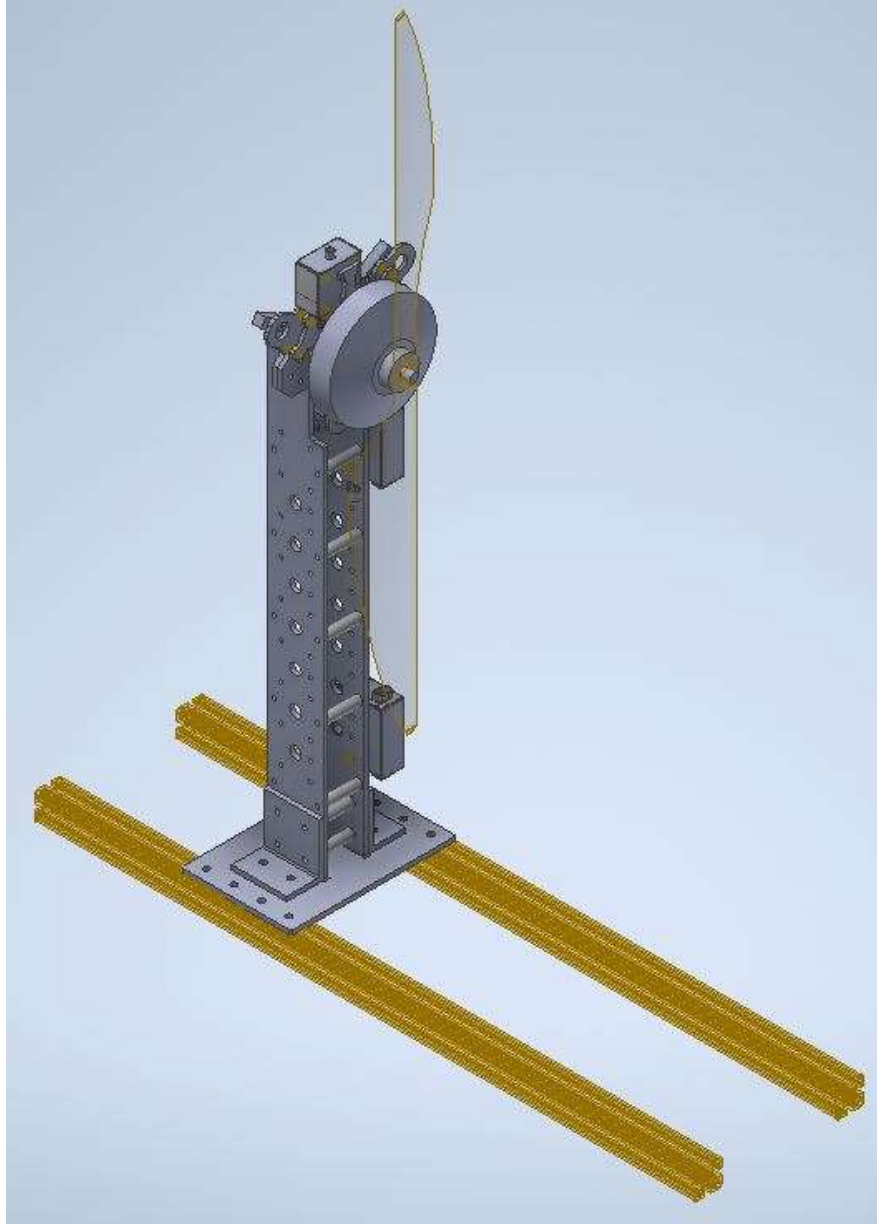


**Figure 22. Series 1780 Test Stand 25 kgf 100-amp: Single Motor**



**Figure 23. Assembled Series 1780 Test Stand 25 kgf 100-amp: Single Motor**

Prior results developed from a previous senior design group will assist in the testing and validation of the propeller test stand. The team performed initial dynamometer pulls to ensure the stand was operating as expected. Tyto Robotics offers an open-source data acquisition software that is user friendly which exports a .csv file of results. These files may be imported into Microsoft Excel for easy manipulation of data. Experimental thrust can be computed at a fixed RPM from the .csv results file and then compared to that of propeller CFD calculations [29]. This allows for a comparison between simulation and experimental results for validation. Stated later in this thesis within Chapter IV. Results and Discussion, iii. Propeller Test Stand, the validation of functionality of the propeller test stand will be compared to that of four APC thin electric propellers. The prior experimental research will serve as a baseline for comparison and replication of results.

The propeller test stand is intended to be used to test large propellers. The current propeller test stand setup has the ability to perform tests on up to 40-inch diameter propellers. With the wind tunnel test section having an internal cross section of 10 feet by 10 feet, the propeller test stand motor mount must be raised to intercept the ideal flow within the wind tunnel. Due to the simple design of the supporting plates the constraint the motor mount, a .dxf file may easily be created to increase the vertical placement of the motor mount to 5 feet. The use of CNC machining will be utilized to cut aluminum  $\frac{1}{4}$  inch thick plates that match that of the exact mounting pattern of the supporting plates. Added hardware will be needed to compensate for these changes in design.

#### **vi. Traversing Section**

The traversing section allows for the measurement of flow during operation and validates the testing. Mounted fore and aft of the test cart area, measurements can be recorded. The initial design of the traversing section was compromised of a 10-foot aluminum 2-inch C-channel, stepper motors, a 10-foot long  $\frac{3}{8}$ -inch diameter acme threaded rod, an aluminum mounting assembly on either side with bearing for the threaded rod to rotate within the C-channel. Within this entire assembly, 3-D printed custom slider mechanisms, 3-D printed custom guides, and two mini slinkys constrain the guides within the C-channel. This entire assembly was constructed and did not operate ideally during preliminary testing. The threaded rod experienced a jump roping effect while being turned. The 3-D printed custom guides did not help as expected. In addition, the developed C-channel had a rough sliding track which often interfered with the 3-D printed custom slider. Figure 24 shows the failed design of the initial traversing mechanism.

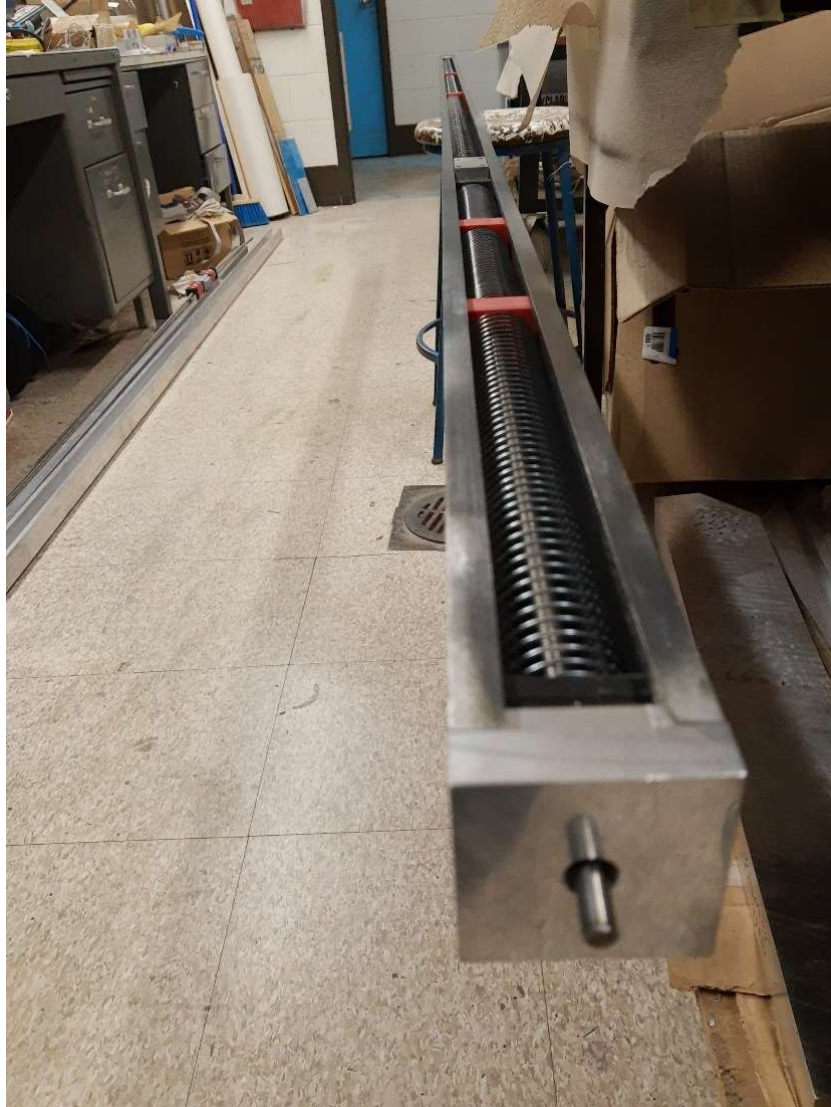


**Figure 24. Initial Traversing Mechanism Design**

Further research led the new design to contain at least a  $\frac{1}{2}$  inch diameter threaded rod. With the increased diameter, the jump roping effect should be minimized during rotation from the stepper motors. The initial design developed will have to be modified to include the change in diameter. To ensure smooth operation of the slider which guides the measurement probes and devices along the test section, the C-channel should be ground to reduce small imperfections in the aluminum.

### **vii. Fan Assembly**

Much thought went into the design and construction of the fan assembly. The assembly is comprised of four 60-inch Drayton fans mounted together in a square configuration each with a 10-horsepower electric motor, belt, and flywheel. In total, the estimated weight of the fan assembly was roughly 2,500 pounds. To begin the assembly, a cart compromised of 2x4's with caster wheels for each fan was constructed to enable work on the fans. They were unable to lay flat on the floor because of the blades protruding slightly outward from the cowling. An engine hoist was utilized with heavy duty straps to lift the fans from their shipping crate onto their carts. The assembled carts with fans could easily be moved independently as needed which aided in the construction due to the weight of each fan/cart assembly being roughly 500 pounds. Each fan/cart assembly was rotated vertically on end to mount the electric motors and flywheels. Referring to the mounting instructions of the electric motors and flywheel, the sub assembly was aligned and secured down on the fans with the provided hardware. Figure 25 shown below represents the fan/cart assembly with mounted motor and flywheel.



**Figure 25. Fan and Cart Assembly with Mounted Motor and Flywheel**

Each cart was moved into position for the square configuration. The edges of the sheet metal from the fans where in contact with another were fixed with nuts and bolts. The carts of each fan were screwed together in numerous locations. Treated 4x4's were cut to length and mounted along the entire perimeter of the fan assembly with carriage bolts. The vertical 4x4's extended the entire length of the assembly whereas the horizontal 4x4's were slightly shorter. This ensures that much of the load experienced is exerted in compression. The horizontal 4x4's would then experience less load and deflection. 6-inch deck screws were utilized at the intersections of each 4x4 beam to secure each end. Upon reflection of the assembly, it was noticed that the distribution of weight upon lifting the entire assembly vertically to mate with the wind tunnel would put a huge moment in the center of the assembly. Buckling of the assembly was expected at the middle seam of the bottom and top set of fans. To counter this, 2x4's were bolted into each side of fans vertically. This would prevent moment created from the motors and flywheels and provide support in compression. These 2x4's were also clamped together on the frame of the fans motor baseplate supports to provided added security. Four eyebolts with 400-pound tensional loading were mounted on the top 4x4 to allow for the crane to attach during the lifting of the assembly. Expected loads of half that of the weight of the total assembly were noted as the base would be supported on the ground during the lift. With the 400-pound eyebolts, the tensional loading would be approximately 1250 pounds. Loading concerns during the lift was the eyebolts deforming the assembly due to the extreme moment created. This could lead to detrimental effects of the performed work. Shown below, Fig. 26 displays the fan assembly on the ground prior to the lift.





**Figure 26. Constructed Fan Assembly prior to Lift**

The fan assembly was lifted in place with the use of an overhead crane mounted on the facility's structural I-beam. During operation, expected vibrations will occur which could lead to significant problems. To counter this, the wind tunnel's structure where the fan assembly would be mated to was secured to the concrete floor to prevent movement. Four 3/8-inch iron 90-degree brackets were made and secured into the concrete and wind tunnel structure. A hammer drill was used and created holes for concrete pins to be placed in each bracket. Bolts secured the wind tunnel structure to the I-beam with nylon nuts. Figures 27 and 28 show the brackets fixed into the concrete and the fully assembled and mated fan assembly. The base of the fan assembly was shimmed with treated 2x4's that had been ripped to the exact height to ensure alignment within the interior of the wind tunnel.





**Figure 27. Mounted Brackets into Concrete**



**Figure 28. Mounted Fan Assembly to Test Section**

### **viii. Multi-Vane Diffuser**

The multi-vane diffuser is comprised of five vanes. Following the fan assembly, a constant cross-sectional of 121 ft<sup>2</sup> is maintained for 6 feet. The constant cross-section is divided up into four equal squares sectioning off each fan independently. ¾ inch smooth plywood was used to construct each divider. Aluminum 90-degree brackets and flat brackets with screws were used to secure and splice the plywood sheets together. The diffuser expands from 11 feet by 11 feet area to max dimensions of 11-feet by 16-feet or 176 ft<sup>2</sup>. The diffuser vanes are proportionally spaced fore and aft of the diffuser. The length of the diffuser spans 8 feet. 2x4's and 2x6's are used to construct the walls, floor, and ceiling. Due to the fans exhausting into the diffuser, OSB sheets were used on all the walls which is not expected to impact the performance of flow within the test section due to the occurring turbulence. The use of 1/8 inch hardboard sheets and 1x4's were used to construct each diffuser vane. The initial frame was secured together using wooden pins. A simple jig was used to bore holes and the wooden pins were secured with wood glue. Due to the actual width of the 1x4's being ¾ inch, the addition of hardboard on either side made the entire diffuser vane have a width of 1 inch. The diffuser vanes were mounted inside the diffuser with ripped 2x4's that were cut at a 45-degree angle to form a triangle. These pieces were secured on top and bottom of each vane on both sides with finishing nails to create a smooth transition. The leading edge of each diffuser contained a blunt edge. A 1-inch diameter wooden dowel rod was cut in half lengthwise and screwed to the entire length of the leading edge to create a smooth transition throughout the diffuser. Since the height of the vanes was 11 feet, the narrow assembly would be subject to vibration during operation of the wind tunnel. To counter this, 3/8-inch diameter threaded rods were custom cut on both the fore and aft side of the vane and secured laterally with a nylon nut compressed into a regular nut. This ensures the threaded rods do not become loose and

hold integrity of the structure. This completed assembly of the diffuser proved to be robust and satisfied requirements. Figure 29 below shows the completed construction of the diffuser.



**Figure 29. Constructed Multi-vane Diffuser Rear View**



## IV. RESULTS AND DISCUSSION

The results from the CFD simulation and an expected experimental results plan has been explained in the following Chapter. The CFD results detail the level of convergence and ensure confidence in the developed postprocessing contours and streamlines. An expected experimental results plan has been detailed for each of the following: validation of both inlet and exit flow, the test cart, propeller thrust stand, and high-speed camera measurements. With the current status of the wind tunnel, this expected experimental results plan will provide information that will be used during initial validation.

### a. CFD Results

#### i. Convergence Criterion

The RMS residuals were created when solving the solution of the fine mesh. A convergence criterion of  $1E-05$  was set over the course of 2000 iterations. With  $1E-05$  level of convergence, the computed results can be acknowledged with confidence. Using the upwind resolution, the solution converged after approximately 1100 iteration. The computation time for this analysis took 40 minutes across 10 processors with 64 gigabytes of RAM. Figure 30 represents the residuals for the conservation of mass and momentum in each direction. The residuals for turbulence are not shown although it also converged within 1100 iterations.

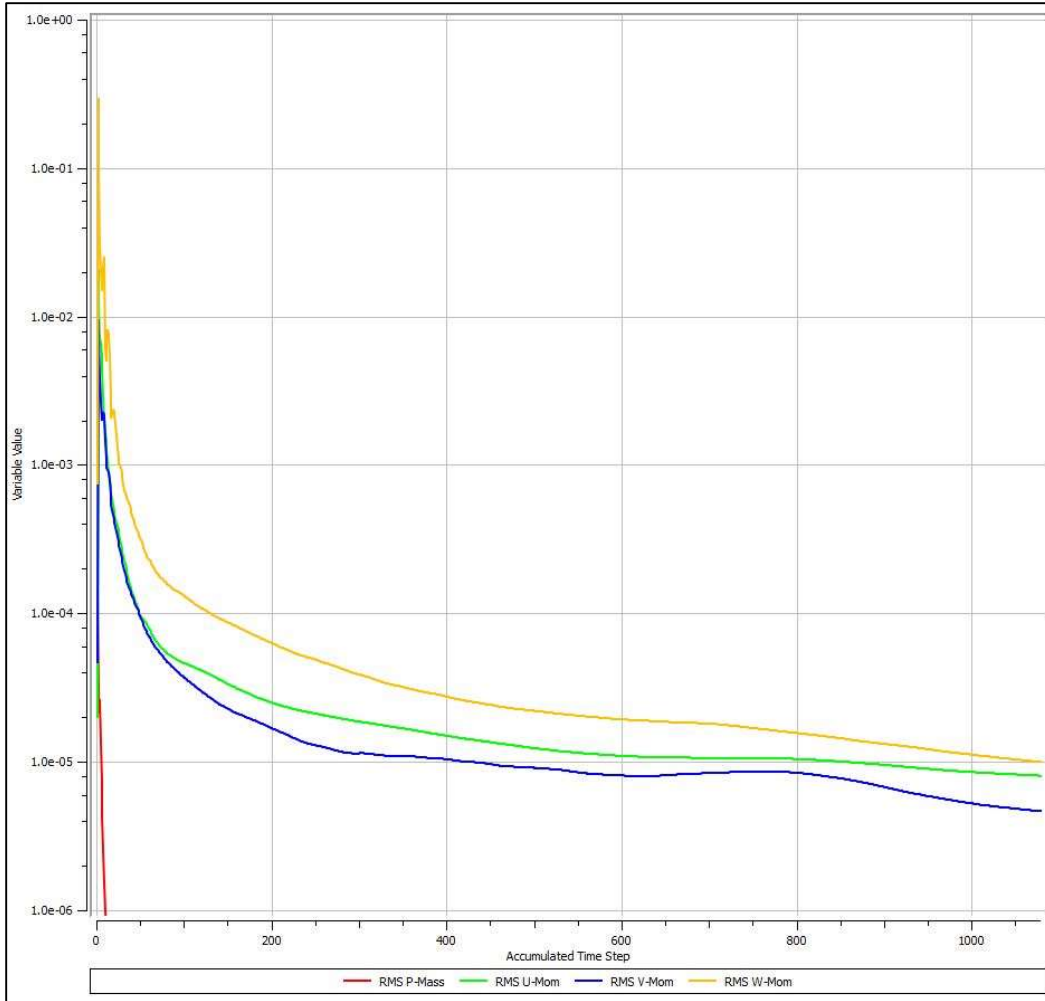
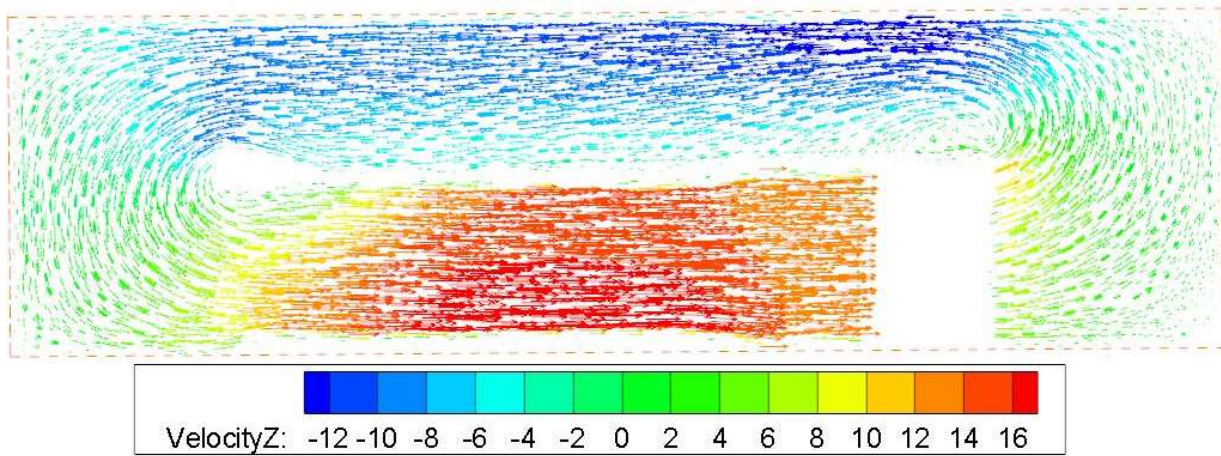


Figure 30. RMS Residuals Convergence of 1E-05

## ii. Postprocessing Results

Postprocessing results of velocity streamlines, velocity contours, and pressure contours were developed to visualize the fluid phenomena occurring throughout the fluid domain. With the use of TecPlot, the plots were developed. As stated above, the fine mesh was used for the postprocessing results. Figure 31 shows the velocity streamlines through the wind tunnel with a slice created at the midpoint of the test section. The velocity streamlines are developed in the z direction, therefore creating a negative magnitude along the top section of the tunnel. These values can be assumed to be positive due to the orientation of the flow.



**Figure 31. Velocity Streamlines at Midpoint in Test Section**

In addition to Fig. 31, another slice was developed within the diffuser to visualize the velocity distribution created. Due to the insertion of the five vanes, the velocity distribution becomes more uniform and does not represent that of a significant parabola. Instead, the vanes direct the flow in a more uniform pattern to allow for reduced effects of the near wall shear stress. Figure 32 represents the streamlines and contours of the wind tunnel with a slice taken at the midpoint of the test section. Orthogonal to this slice, another slice is developed within the diffuser vanes with velocity contours. Again, note that the velocity is in the z direction, therefore one can assume the negative values produced are positive.

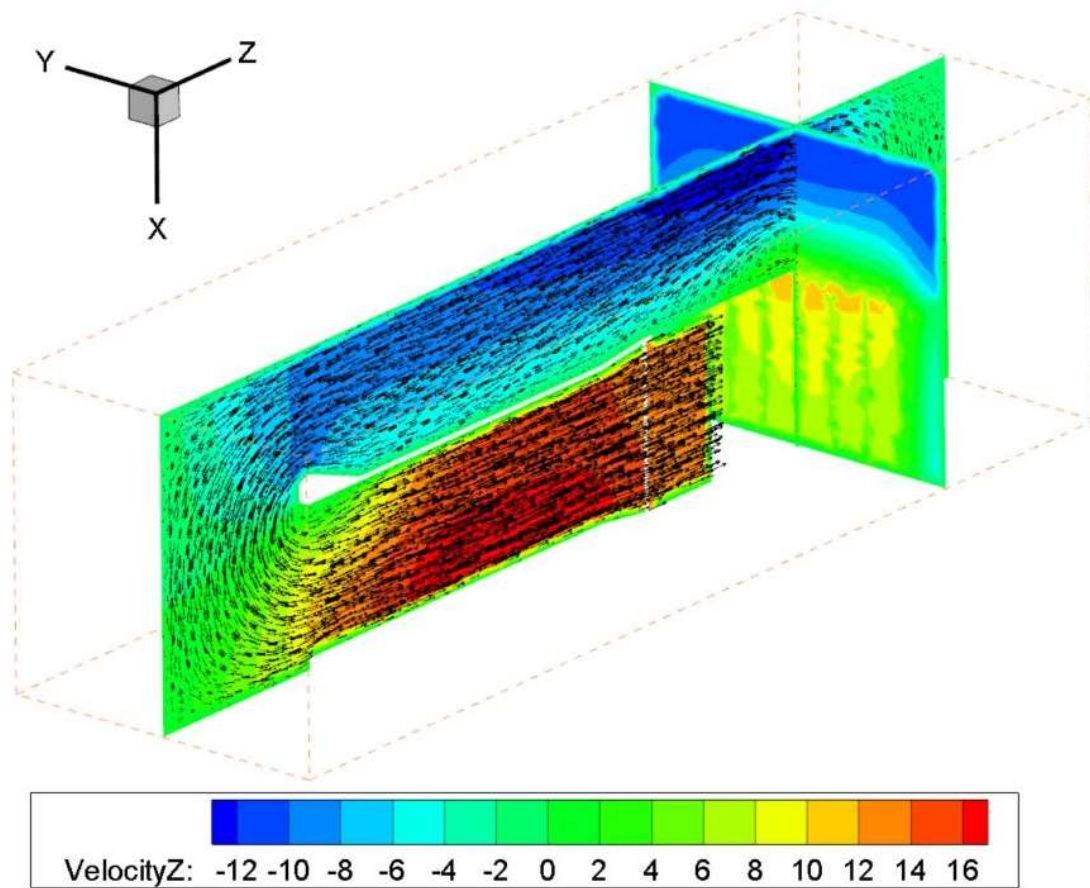


Figure 32. Velocity Streamlines and Contours within Test Section and Diffuser

Pressure contours were developed to further analyze the flow uniformity in the wind tunnel as well as the test section pressure. Figure 33 shown below represents the pressure distribution created. This is shown at the midpoint within the test section just as Fig. 31 and 32 with the velocity streamlines. Within Fig. 33, one can see that effects of the near wall and the increase of pressure created from the induced air flow created from the driving fans. The pressure returns to that of atmospheric conditions within the test section due to the contraction of the inlet. Note that the middle vane inserted within the diffuser impacts the pressure contours due to the placement of the slice.

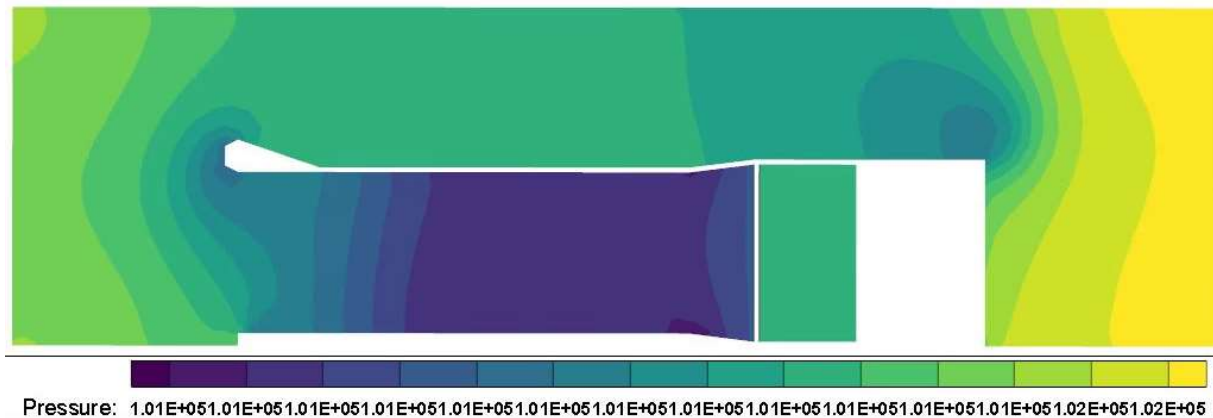


Figure 33. Pressure Contours at Midpoint in Test Section

## b. Expected Experimental Results Plan

### i. Validation of Inlet and Exit Flow

The validation of the inlet and exit flow will be completed by performing a full inlet and exit total pressure survey. This will provide a measurement of the flow uniformity on either side of the test section. A measuring array will be constructed that will span 2 feet with a total of 24 total pressure probes. These will be connected to individual piezo-resistive pressure sensors that will then supply signals to the data acquisition system. This process will be repeated throughout the entire area of the inlet and exit areas to develop a mapped grid each with an experimental measurement with the desired goal of uniformity. The total pressure losses will be determined through the difference between fore and aft locations within the test section. The effects of the near wall creating a boundary layer will be examined on each wall within the wind tunnel. The completed validation of inlet and exit flows will ensure the wind tunnel is operating as expected.



## ii. Test Cart

Currently, the test cart will be configured to measure drag, thrust, and downforce. Four 100 kg force load cells are being used for the downforce measurement. These load cells have an accuracy of 0.02%. They are powered through a 10 VDC source. The sensor output of 3 mV/V will send a signal to the data acquisition system for measurement. To initially test calibration of the load cells, calibrated weights can be used to ensure accuracy. A large cylinder in cross flow experiment would allow for a simple approach for ensuring the load cells measure the correct drag induced. The skin friction created from the test cart at 30 mph computes to approximately 1.4 N. During operation, the difference between the measured drag of the cylinder and drag due to skin friction created from the test cart can be used as a comparison between the theoretical drag. The use of more sensitive load cells should be considered when testing smaller aerodynamic profiles and propellers. The primary measurement of thrust from the propeller stand can be compared to the value acquired from the test cart. used as a comparison to that of the test cart.

## iii. Propeller Test Stand

To validate the functionality of the propeller test stand, four APC thin electric propellers (14x12E, 17x12E, 19x12E, 27x13E) with prior research documented within Brant and Selig will be tested to ensure the replication of results [30]. Exit surveys downstream of the propeller will be used to experimentally acquire jet power. The following equations (7-10) will be used to estimate the advance ratio and efficiencies:

$$J = \frac{v}{nD} \quad (7)$$

$$\eta_{overall} = \frac{\text{Thrust Power}}{\text{Mechanical Power}} \quad (8)$$

$$\eta_{propulsion} = \frac{Thrus\ Power}{Jet\ Power} \quad (9)$$

$$\eta_{propellor} = \frac{Jet\ Power}{Mechanical\ Power} \quad (10)$$

#### iv. High Speed Camera Measurements

The use of a high-speed camera will be utilized for recording deflection, distortion, and vibration measurements. The high-speed camera will also be used to investigate the feasibility of pressure sensitive paint (PSP). Traditionally, embedded arrays of pressure taps are used for acquiring pressure distributions. This process is tedious and only provides a limited resolution of results. PSPs are a non-contact technique of measurement; therefore, it is suitable to perform measurements on highspeed rotation blades [31]. A grid may be painted on the propeller to distinguish differences. High-speed bursts of the camera triggered at the same rotational locations will be used to make one to one comparisons of images to acquire time dependent results of deflection, distortion, and vibration.

## V. RECOMMENDATIONS

Future work should be performed on the CFD analysis to farther refine results. The generation of a more refined mesh throughout the fluid domain and near critical areas of the wind tunnel should be created to predict the flow more accurately. The addition of a flow straightener can be added by inducing a pressure drop and direct flow at the front of the inlet contraction. There will be vorticity due to the 180-degree turn into the inlet. This will eliminate the turbulent eddies and produce a desired uniform low turbulence flow within the test section. Although with the addition of the flow straightener, computational costs will be increased magnitudes greater due to the required mesh that would have to be developed. Any farther modifications performed on the real-world structure can be updated within the simulation to ensure the produced results match that of the experimental. Desired convergence criterion of 1E-06 should be attempted although the computation costs of a more refined mesh will generate significant amounts of time and RAM required with the increased level of convergence. The use of a powerful workstation should be used after the enhancement of the mesh resolution to expedite the computation of results.

Future work will be required to better improve wind tunnel performance. The addition of walls to partition off the wind tunnel facility from the rest of the building will ensure the facility is a closed-loop tunnel. Since there will not be turning vanes at the corners, the inlet and exit walls of the buildings structure should have a smooth profile curve added to better direct the air around the 180 degree turns. Future work could incorporate turning vanes into the design although challenging as well as increasing the radius between the top and bottom flows. The impeding I-beams for the ceiling support should have a structure built to make it more profile and streamline. The beams will induce tripping of the boundary layer and create more turbulent air upon entering the flow conditioning and inlet of the wind tunnel. The curved profile at the inlet to assist the flow

to turn is recommended based upon the CFD results developed. Time should be spent repairing any leaks that are noticed. This will improve the performance overall. The top of the wind tunnel's ceiling still has the wood framing exposed. OSB sheets are recommended to be attached to smooth out this section and allow for better streamlining of the flow. Further thought must be contributed to the full operation of the traversing section. Until this section is developed, experimental results cannot be validated.

## VI. CONCLUSION

Within the CFD analysis, a geometry was created to match that of the real-world structure currently being developed. The geometry matched that of the real-world structure with a few assumptions such as the flat roof and curved inlet top. These will eventually be added to the real-world model in time, so this analysis proves to be a sufficient representation of the soon to be constructed wind tunnel. With the use of the mesh interdependence study, the computational costs were evaluated as well as the accuracy of the results. With the developed analytical solution, the simulated results of each mesh were compared to decide which mesh would prove to provide the best results. Using a convergence criterion of  $1E-05$ , the confidence within the results can be acknowledged. The postprocessing results developed accurately represent that of expectations and visually show the expected flow phenomena occurring throughout the fluid domain. The velocity streamlines and contours through the diffuser show an ideal representation of the exit velocity profile by producing a more uniform distribution than that of a diffuser without inserted vanes.

The design, development, and validation of the design have all been described in detail. The flow conditioning, inlet contraction, test section, traversing section, test cart, propeller test stand, and multi-vane diffuser sections cover the processes used to construct each. A comparison between analytical calculations and a proposed experimental procedure will be used to validate the functionality. The test cart and propeller test stand will need to be finished before continuing. The steps outlined within Chapter IV walk through the requirements to produce ideal results. Once complete, the wind tunnel facility will be used to test assorted propeller/motor configurations in the single configuration. Continued research will occur in line with the NAVY to achieve a better understanding of propeller losses in regard to UAV's. Departments throughout the University may also conduct research within the facility to support their work.

## REFERENCES

- <sup>1</sup>“High Efficiency Propeller for Small Unmanned X Systems using Advanced Composite Materials,” Phase I Grant, Catto Propellers., U.S. Navy., University of North Dakota., Grand Forks, ND, Oct. 2021.
- <sup>2</sup>Barlow, J.B., Rae, W.H. Jr. and Pope, A. *Low-Speed Wind Tunnel Testing* (3rd ed.), John Wiley and Sons, NY, 1999, pp. 37-50.
- <sup>3</sup>Jaramillo, J.D. “Design and Construction of a Low-Speed Wind Tunnel,” B.S. Thesis, Department of Physics., Houghton College., Houghton, NY, 2017.
- <sup>4</sup>Kaplan, B. “The Design, Fabrication, and Evaluation of a Low-Speed, Low-Turbulence, Anechoic Wind Tunnel,” M.S. Thesis, Department of Aerospace Engineering., Embry-Riddle Aeronautical University., Daytona Beach, FL, 1996.
- <sup>5</sup>Mehta, R.D. “Aspects of the Design and Performance of Blower Tunnel Components,” Ph.D. Thesis, Department of Aeronautics., Imperial College London University., London, UK, Nov. 1978, pp. 3-5.
- <sup>6</sup>Watmuff, J.H. “Detrimental Effects of Almost Immeasurably Small Freestream Nonuniformities Generated by Wind Tunnel Screens,” *American Institute of Aeronautics and Astronautics Journal.*, 36(3), 1998, pp. 379-386.
- <sup>7</sup>Kulkarni, V., Sahoo, N., Chavan, S.D., “Simulation of Honeycomb-Screen Combinations for Turbulence Management in a Subsonic Wind Tunnel,” *Journal of Wind Engineering and Industrial Aerodynamics.*, Vol. 99, 2011, pp. 37-45, <https://doi.org/10.1016/j.jweia.2010.10.006>.
- <sup>8</sup>Eckert, W.T., Mort, K.W., Joep, J. “Aerodynamics Design Guidelines and Computer Program for Estimation of Subsonic Wind Tunnel Performance,”
- <sup>9</sup>Cattafesta, L., Bahr, C., & Mathew, J. “Fundamentals of Wind-Tunnel Design. In *Encyclopedia of Aerospace Engineering.*” John Wiley and Sons, 2010, <https://doi.org/10.1002/9780470686652.eae532>.
- <sup>10</sup>Morel T. “Comprehensive Design of Axisymmetric Wind Tunnel Contractions,” *Journal of Fluids Engineering.*, 97(2), 1975, pp. 225-233.
- <sup>11</sup>Healzer, J.M., Moffat, R.J., Kays, W.M. “The Turbulent Boundary Layer on a Rough Porous Plate: Experimental Heat Transfer with Uniform Blowing,” Ph. D. Thesis, Department of Mechanical Engineering., Stanford University., Stanford, CA, May 1974.
- <sup>12</sup>Mehta, R.D. and Bradshaw, P. “Design Rules for Small Low Speed Wind Tunnels,” *Aeronautical Journal.*, 83, 1979, pp. 443-449.
- <sup>13</sup>Lefebvre, A. H., Ballal D.R. *Gas Turbine Combustion: Alternative Fuels and Emissions* (3<sup>rd</sup> ed.) Boca Raton, FL: CRC Press, 2010, pp. 87-90.
- <sup>14</sup>Meng, X., Zuo, Z., Nishi, M., and Liu, S. “A Numerical Study on the Flow Mechanism of Performance Improvement of a Wide-Angle Diffuser by Inserting a Short Splitter vane. *Multidisciplinary Digital Publishing Institute.*, 8(2)., 2020, <https://doi.org/10.3390/pr8020143>.
- <sup>15</sup>Calautit, J.K., Chaudhry, H.N., Hughes, B.R., Sim, L.F. “A Validated Design Methodology for a Closed-Loop Subsonic Wind Tunnel,” *Journal of Wind Engineering and Industrial Aerodynamics.*, Vol. 125, 2014, pp. 180-194, <https://doi.org/10.1016/j.jweia.2013.12.010>.
- <sup>16</sup>Schubauer, G.B., Spangenberg W.G., Klebanoff, P.S. “Aerodynamic Characteristics of Damping Screens,” *National Advisory Committee for Aeronautics.*, Technical Note 2001, Jan. 1950.

<sup>17</sup> Schubauer, G.B., Spangenberg W.G. “Effect of Screens in Wide-Angle Diffusers,” National Advisory Committee for Aeronautics., Technical Note 1610, July 1948.

<sup>18</sup> Sargison, J.E., Walker, G.J., Rossi, R. “Design and Calibration of a Wind Tunnel with a Two-Dimensional Contraction,” School of Engineering., University of Tasmania., Sydney, ASTL, Dec. 2004.

<sup>19</sup> Johnson, D.A., King, L.S. “A Mathematically Simple Turbulence Closure Model for Attached and Separated Turbulent Boundary Layers,” American Institute of Aeronautics and Astronautics Journal., NASA Ames Research Center, Moffett Field, CA, 23(11), Nov. 1985.

<sup>20</sup> Menter, F.R. “Two-Equation Eddy-Viscosity Turbulence Models for Engineering Applications,” American Institute of Aeronautics and Astronautics Journal., 32(8), Aug. 1994.

<sup>21</sup> Wilcox, D.C. “Reassessment of the Scale-Determining Equation for Advanced Turbulence Models,” American Institute of Aeronautics and Astronautics Journal., DCW Industries, Inc., La Canada, CA, 26(11), Nov. 1988.

<sup>22</sup> Rumsey, C. “Turbulence Modeling Resource Menter Shear Stress Transport Turbulence Model,” NASA Langley Research Center, Mar. 2021.

<sup>23</sup> Deters, R. W., Ananda G.K., Selig, M.S. “Slipstream Measurements of Small-Scale Propellers at Low Reynolds Numbers,” Embry-Riddle Aeronautical University., Daytona Beach, FL, University of Illinois at Urbana-Champaign., Urbana, IL, June, 2015, <https://doi.org/10.2514/6.2015-2265>.

<sup>24</sup> Bramwell, A. R. S., *Helicopter Dynamics*. Ney York, NY. John Wiley and Sons, 1976.

<sup>25</sup> Robertson, J. A., Elger, D. F., LeBret, B. A., & Crowe, C. T. *Engineering Fluid Mechanics* (11th ed.). Hoboken, NJ: John Wiley & Sons, 2014.

<sup>26</sup> Ames, F.E. *An Introduction to Compressible Fluid Flow*. New York, NY. Momentum Press LLC, 2018 pp. 52-54.

<sup>27</sup> Matejka, A., Moyer, N., Schroetlin, H., “Large Scale Wind Tunnel,” Senior Design Report, Department of Mechanical Engineering., University of North Dakota., Grand Forks, ND, May 2021.

<sup>28</sup> “Series 1780 25 & 40 kg Test Stand User Manual V3.0,” Tyto Robotics., Gatineau, QC, Canada, July 2021, [tytorobotics.com](http://tytorobotics.com).

<sup>29</sup> Drayna, Z., Molde, S., Syrstad, M., Salaam., L. “Mobile Recon System Blade Optimization,” Senior Design Report, Department of Mechanical Engineering., University of North Dakota., Grand Forks, ND, May, 2021.

<sup>30</sup> Shetty, O.R., Selig, M.S. “Small-Scale Propellers Operating in the Vortex Ring State,” Department of Aerospace Engineering., University of Illinois at Urbana-Champaign., Urbana, IL, Jan. 2011.

<sup>31</sup> Jahanmiri, M. “Pressure Sensitive Paints: The Basic Principles and Practical Applications,” Department of Mechanical and Aerospace Engineering., Shiraz University of Technology., Shiraz, Iran, April, 2015.

APPENDIX A

Table 2. "S" Shape Curve Inlet Contraction Dimensions (1 of 3)

X-Distance	Y-Distance	X-from test section	Y from test section	Total opening of inlet	Y distance(inches)	Total Distance of Curve
<b>38</b>	<b>5.0031829</b>	<b>0</b>	<b>0.003182904</b>	<b>10.00636581</b>	<b>0.038194846</b>	<b>0.003182904</b>
38.0833333	5.00433215	0.083333333	0.004332152	10.0086643	0.05198582	0.086524161
38.1666667	5.00575764	0.166666667	0.005757642	10.01151528	0.069091706	0.169869686
38.25	5.0074967	0.25	0.0074967	10.0149934	0.089960395	0.253221163
38.3333333	5.00958799	0.333333333	0.009587988	10.01917598	0.115055858	0.336580733
38.4166667	5.01207134	0.416666667	0.012071336	10.02414267	0.144856033	0.419951061
38.5	5.01498756	0.5	0.014987564	10.02997513	0.179850769	0.503335405
38.5833333	5.01837832	0.583333333	0.018378318	10.03675664	0.220539814	0.586737693
38.6666667	5.0222859	0.666666667	0.022285904	10.04457181	0.26743085	0.670162591
38.75	5.02675313	0.75	0.026753132	10.05350626	0.321037582	0.753615575
38.8333333	5.03182316	0.833333333	0.031823156	10.06364631	0.381877874	0.837102997
38.9166667	5.03753933	0.916666667	0.037539328	10.07507866	0.450471931	0.920632148
<b>39</b>	<b>5.04394504</b>	<b>1</b>	<b>0.043945045</b>	<b>10.08789009</b>	<b>0.527340535</b>	<b>1.004211318</b>
39.0833333	5.05108361	1.083333333	0.05108361	10.10216722	0.613003325	1.087849847
39.1666667	5.05899809	1.166666667	0.058998094	10.11799619	0.70797713	1.171558171
39.25	5.0677312	1.25	0.067731196	10.13546239	0.812774348	1.255347857
39.3333333	5.07732511	1.333333333	0.077325115	10.15465023	0.927901378	1.339231632
39.4166667	5.08782142	1.416666667	0.087821424	10.17564285	1.053857093	1.4232234
39.5	5.09926095	1.5	0.099260948	10.1985219	1.191131372	1.507338245
39.5833333	5.11168364	1.583333333	0.111683639	10.22336728	1.340203673	1.59159243
39.6666667	5.12512847	1.666666667	0.125128471	10.25025694	1.501541657	1.676003377
39.75	5.13963332	1.75	0.139633322	10.27926664	1.675599868	1.760589635
39.8333333	5.15523487	1.833333333	0.155234871	10.31046974	1.862818448	1.84537084
39.9166667	5.17196849	1.916666667	0.171968493	10.34393699	2.063621911	1.930367655
<b>40</b>	<b>5.18986816</b>	<b>2</b>	<b>0.189868164</b>	<b>10.37973633</b>	<b>2.278417969</b>	<b>2.015601702</b>
40.0833333	5.20896637	2.083333333	0.208966366	10.41793273	2.507596393	2.101095478
40.1666667	5.22929399	2.166666667	0.229293995	10.45858799	2.751527937	2.186872264
40.25	5.25088028	2.25	0.250880276	10.50176055	3.010563307	2.272956013
40.3333333	5.27375268	2.333333333	0.273752681	10.54750536	3.28503217	2.35937124
40.4166667	5.29793685	2.416666667	0.297936852	10.5958737	3.575242227	2.446142886
40.5	5.32345653	2.5	0.323456527	10.64691305	3.881478323	2.533296189
40.5833333	5.35033347	2.583333333	0.350333468	10.70066694	4.204001612	2.620856536
40.6666667	5.3785874	2.666666667	0.378587397	10.75717479	4.543048769	2.708849314
40.75	5.40823594	2.75	0.408235937	10.81647187	4.898831248	2.797299754
40.8333333	5.43929455	2.833333333	0.43929455	10.8785891	5.271534598	2.886232773
40.9166667	5.47177648	2.916666667	0.471776485	10.94355297	5.661317816	2.975672812
<b>41</b>	<b>5.50569273</b>	<b>3</b>	<b>0.50569273</b>	<b>11.01138546</b>	<b>6.068312757</b>	<b>3.065643675</b>



Table 3. "S" Shape Curve Inlet Contraction Dimensions (2 of 3)

41	5.50569273	3	0.50569273	11.01138546	6.068312757	3.065643675
41.0833333	5.54105197	3.083333333	0.541051966	11.08210393	6.492623594	3.156168368
41.1666667	5.57786053	3.166666667	0.577860527	11.15572105	6.934326319	3.247268942
41.25	5.61612236	3.25	0.616122358	11.23224472	7.393468299	3.338966336
41.3333333	5.65583899	3.333333333	0.65583899	11.31167798	7.870067881	3.431280232
41.4166667	5.6970095	3.416666667	0.697009504	11.39401901	8.364114045	3.524228904
41.5	5.73963051	3.5	0.739630508	11.47926102	8.875566101	3.617829088
41.5833333	5.78369612	3.583333333	0.783696121	11.56739224	9.404353446	3.712095851
41.6666667	5.82919795	3.666666667	0.829197947	11.65839589	9.950375359	3.807042471
41.75	5.87612507	3.75	0.876125071	11.75225014	10.51350085	3.902680327
41.8333333	5.92446405	3.833333333	0.924464046	11.84892809	11.09356856	3.999018798
41.9166667	5.97419889	3.916666667	0.974198891	11.94839778	11.69038669	4.096065174
42	6.02531109	4	1.025311087	12.05062217	12.30373304	4.193824578
42.0833333	6.07777958	4.083333333	1.077779583	12.15555917	12.9333355	4.292299892
42.1666667	6.13158081	4.166666667	1.131580806	12.26316161	13.57896967	4.391491707
42.25	6.18668867	4.25	1.186688668	12.37337734	14.24026401	4.491398267
42.3333333	6.24307458	4.333333333	1.243074584	12.48614917	14.91689501	4.592015443
42.4166667	6.30070749	4.416666667	1.300707495	12.60141499	15.60848994	4.693336698
42.5	6.35955389	4.5	1.359553886	12.71910777	16.31464664	4.795353081
42.5833333	6.41957782	4.583333333	1.419577821	12.83915564	17.03493385	4.898053213
42.6666667	6.48074097	4.666666667	1.480740968	12.96148194	17.76889162	5.001423301
42.75	6.54300264	4.75	1.543002643	13.08600529	18.51603171	5.105447147
42.8333333	6.60631984	4.833333333	1.606319842	13.21263968	19.2758381	5.210106175
42.9166667	6.67064729	4.916666667	1.670647293	13.34129459	20.04776751	5.315379464
43	6.7359375	5	1.7359375	13.471875	20.83125	5.42124379
43.0833333	6.8021408	5.083333333	1.802140798	13.6042816	21.62568958	5.527673679
43.1666667	6.86920541	5.166666667	1.869205407	13.73841081	22.43046489	5.63464146
43.25	6.9370775	5.25	1.937077497	13.87415499	23.24492996	5.742117341
43.3333333	7.00570125	5.333333333	2.005701247	14.01140249	24.06841496	5.850069476
43.4166667	7.07501892	5.416666667	2.075018919	14.15003784	24.90022703	5.958464052
43.5	7.14497093	5.5	2.14497093	14.28994186	25.73965116	6.067265377
43.5833333	7.21549593	5.583333333	2.215495925	14.43099185	26.58595111	6.176435975
43.6666667	7.28653087	5.666666667	2.286530866	14.57306173	27.43837039	6.285936693
43.75	7.35801111	5.75	2.358011109	14.71602222	28.2961333	6.395726809
43.8333333	7.4298705	5.833333333	2.429870497	14.85974099	29.15844597	6.505764149
43.9166667	7.50204146	5.916666667	2.502041456	15.00408291	30.02449747	6.616005211
44	7.57445509	6	2.574455088	15.14891018	30.89346105	6.726405294
44.0833333	7.64704127	6.083333333	2.647041273	15.29408255	31.76449527	6.836918636

Table 4. "S" Shape Curve Inlet Contraction Dimensions (3 of 3)

45	8.43593964	7	3.435939643	16.87187929	41.23127572	8.046344794
45.08333333	8.50483932	7.083333333	3.504839316	17.00967863	42.0580718	8.15447254
45.16666667	8.57294254	7.166666667	3.572942544	17.14588509	42.87531052	8.262094536
45.25	8.64017506	7.25	3.640175062	17.28035012	43.68210075	8.36916767
45.33333333	8.7064634	7.333333333	3.706463402	17.4129268	44.47756082	8.475650478
45.41666667	8.77173505	7.416666667	3.77173505	17.5434701	45.2608206	8.581503359
45.5	8.83591862	7.5	3.835918625	17.67183725	46.0310235	8.686688794
45.58333333	8.89894405	7.583333333	3.898944047	17.79788809	46.78732857	8.79117156
45.66666667	8.96074272	7.666666667	3.960742723	17.92148545	47.52891268	8.894918949
45.75	9.02124772	7.75	4.021247724	18.04249545	48.25497268	8.997900984
45.83333333	9.08039397	7.833333333	4.080393975	18.16078795	48.9647277	9.100090629
45.91666667	9.13811845	7.916666667	4.138118447	18.27623689	49.65742137	9.201463994
46	9.19436035	8	4.194360352	18.3887207	50.33232422	9.302000535
46.08333333	9.24906134	8.083333333	4.249061338	18.49812268	50.98873606	9.401683244
46.16666667	9.3021657	8.166666667	4.302165702	18.6043314	51.62598842	9.500498819
46.25	9.35362059	8.25	4.353620586	18.70724117	52.24344703	9.598437828
46.33333333	9.4033762	8.333333333	4.403376198	18.8067524	52.84051438	9.69549485
46.41666667	9.45138602	8.416666667	4.451386023	18.90277205	53.41663228	9.791668587
46.5	9.49760705	8.5	4.497607046	18.99521409	53.97128455	9.886961962
46.58333333	9.54199997	8.583333333	4.54199997	19.08399994	54.50399963	9.981382173
46.66666667	9.58452945	8.666666667	4.58452945	19.1690589	55.0143534	10.07494072
46.75	9.62516432	8.75	4.625164324	19.25032865	55.50197189	10.16765338
46.83333333	9.66387785	8.833333333	4.663877846	19.32775569	55.96653416	10.25954016
46.91666667	9.70064793	8.916666667	4.70064793	19.40129586	56.40777516	10.3506252
47	9.73545739	9	4.73545739	19.47091478	56.82548868	10.44093656
47.08333333	9.76829419	9.083333333	4.768294194	19.53658839	57.21953032	10.53050609
47.16666667	9.79915171	9.166666667	4.799151709	19.59830342	57.58982051	10.61936908
47.25	9.82802897	9.25	4.828028967	19.65605793	57.9363476	10.70756398
47.33333333	9.85493092	9.333333333	4.854930915	19.70986183	58.25917099	10.79513201
47.41666667	9.87986869	9.416666667	4.87986869	19.75973738	58.55842428	10.88211167
47.5	9.90285988	9.5	4.902859879	19.80571976	58.83431854	10.96856344
47.58333333	9.9239288	9.583333333	4.923928796	19.84785759	59.08714555	11.05451892
47.66666667	9.94310676	9.666666667	4.943106761	19.88621352	59.31728113	11.14003055
47.75	9.96043238	9.75	4.960432375	19.92086475	59.5251885	11.22514589
47.83333333	9.97595181	9.833333333	4.975951812	19.95190362	59.71142174	11.30991202
47.91666667	9.9897191	9.916666667	4.989719101	19.9794382	59.87662922	11.39437493
48	10.0017964	10	5.001796426	20.00359285	60.02155711	11.47857888
49	10	11	5	20	60	12.4785805